

1 Revisiting The Rare Transition of a South Atlantic  
2 Cyclone to Tropical Storm Akará: Energy Cycle  
3 and Stratosphere-Troposphere Interaction

4 Danilo Couto de Souza<sup>1,2\*</sup>, Victor Antunes Ranieri<sup>1</sup>,  
5 Pedro Leite da Silva Dias<sup>1</sup>, Andres Rodríguez Flores<sup>1</sup>,  
6 Ricardo Camargo<sup>1</sup>

7 <sup>1</sup>\*Institute of Astronomy, Geophysics and Atmospheric Sciences, São  
8 Paulo University, Rua do Matão, 266, São Paulo, 05508-090, São Paulo,  
9 Brazil.

10 <sup>2</sup>Climate Risk Initiative, IRB(re), Av. República do Chile, 330 - 40  
11 andar, Rio de Janeiro, 20031-170, Rio de Janeiro, Brazil.

12 \*Corresponding author(s). E-mail(s): [danilo.oceano@gmail.com](mailto:danilo.oceano@gmail.com)<sup>✉</sup>;  
13 Contributing authors: [victor.ranieri@usp.br](mailto:victor.ranieri@usp.br)<sup>✉</sup>; [pldsdias@gmail.com](mailto:pldsdias@gmail.com)<sup>✉</sup>;  
14 [arodriguez@usp.br](mailto:arodriguez@usp.br)<sup>✉</sup>; [ricamarg@usp.br](mailto:ricamarg@usp.br)<sup>✉</sup>;

15 **Abstract**

16 Cyclone Akará was the third documented tropical cyclone in the South Atlantic,  
17 undergoing a rare subtropical-to-tropical transition in February 2024. This study  
18 investigates the dynamical, thermodynamical, and energetic evolution of Akará  
19 using a diagnostic framework combining the Lorenz Energy Cycle (LEC) and  
20 heat and vorticity budgets. Akará originated in a post-frontal, weakly baroclinic  
21 environment characterized by warm sea surface temperatures ( $> 28^{\circ}\text{C}$ ), strong  
22 ocean-atmosphere thermal contrast, and low vertical wind shear. These condi-  
23 tions favored convective activity and led to the development of a symmetric  
24 warm core, initially supported by latent heat release and interaction with an  
25 upper-level cutoff low. As the system intensified, it transitioned into a tropical  
26 cyclone, exhibiting a deep warm core and organized convection. Stratospheric  
27 air intrusions were identified during and after the tropical transition, contribut-  
28 ing to upper-tropospheric warming and enhancing cyclone intensification. Heat  
29 and vorticity budget analyses revealed how vertical motion, latent heat release,  
30 and vortex stretching shaped the storm's three-dimensional structure and con-  
31 tributed to its deepening. During the mature stage, Akará reached peak intensity  
32 while moving over cooler waters. Although convective activity decreased, the

warm core was sustained—likely through continued stratosphere-troposphere interactions and strong barotropic energy conversions at low and mid levels. The combined use of LEC and budget diagnostics proved effective in disentangling the physical mechanisms behind Akar  's evolution, offering valuable insight into the dynamics of rare South Atlantic tropical transitions. Expanding such analyses to other events is essential to improve our understanding and forecasting of tropical cyclogenesis in this basin.

**Keywords:** Tropical Transition, South Atlantic Cyclones, Lorenz Energy Cycle, Stratosphere-Troposphere Interaction, Heat and Vorticity Budgets, Barotropic Conversions, Latent Heat Release

## Acknowledgements

This study was partly financed by the Coordena  o de Aperfei  amento de Pessoal de N  vel Superior – Brasil (CAPES) under Finance Code 001. The authors would like to thank the Laboratory of Applied Meteorology for Regional Meteorological Systems (MASTER) for providing the data processing infrastructure. Special thanks are extended to Jean Peres and Djalma Vieira for their invaluable technical assistance and support in the laboratory, which contributed significantly to the success of this research.

## 1 Introduction

South America contains several hot spots for cyclogenesis (Gan and Rao, 1991; Reboita et al., 2010; Gramcianinov et al., 2019; de Souza et al., 2024). Most of these cyclones are extratropical (Marrafon et al., 2022), while some, particularly near South-eastern Brazil, are subtropical (Gozzo et al., 2014, 2017). Tropical cyclones are rare in the South Atlantic basin due to unfavorable environmental conditions, such as relatively cool sea surface temperatures (SST) and high vertical wind shear (Pezza and Simmonds, 2005). While high SST (above 26.5°C) provides the necessary heat and moisture to fuel deep convection, low vertical wind shear is essential to maintain the system's structural coherence, allowing the cyclone to intensify and sustain its warm-core structure (Gray, 1968; Emanuel, 1986; Davis and Bosart, 2003; Rios-Berrios et al., 2024). Despite these unfavorable conditions, a peak in the Genesis Potential Index (GPI), a necessary but not sufficient condition for tropical cyclogenesis, has been identified near the Southeastern Brazilian coast (Camargo et al., 2007), particularly during March (Andrelina Silva and Sim  es Reboita, 2021).

Tropical transition refers to the process in which an extratropical or subtropical cyclone develops a deep warm core, thereby acquiring the status of a tropical cyclone (Davis and Bosart, 2003; Wood et al., 2023). In the South Atlantic, subtropical cyclogenesis is primarily driven by upper-level blocking patterns, the presence of mid-upper level troughs or cutoff-lows, and air-sea interactions involving heat fluxes and moisture transport from remote sources, specially from the South Atlantic Subtropical High

(SASH) (Gozzo et al., 2014, 2017). Once a subtropical cyclone forms, various atmospheric and oceanic conditions can influence its evolution into a tropical cyclone. Key factors such as sea surface temperature anomalies, isolation from baroclinic influences, persistent heat fluxes from the ocean, and dynamic processes that reduce vertical wind shear are critical in facilitating tropical transition of subtropical cyclones (da Rocha et al., 2019). However, it is important to note that tropical transition mechanisms may vary even within different regions of the same ocean basin (Wood et al., 2023). Despite the growing interest in understanding tropical transition, most research has been conducted in the Northern Atlantic (Wood et al., 2023), leaving significant gaps in knowledge regarding the South Atlantic, where tropical transitions are less frequent and less understood.

In addition to air-sea interactions, troposphere-stratosphere interactions can also influence tropical cyclone development. Vigorous convective activity during a tropical cyclone's life cycle can induce stratospheric air intrusions into the troposphere, as the cyclone inflow may penetrate the lower stratosphere (Moon and Kieu, 2017; Barnes et al., 2022; Ohno and Satoh, 2015). These intrusions bring high potential vorticity air into the upper troposphere, which can enhance surface cyclogenesis, as described by Hoskins et al. (1985). Furthermore, deep convection associated with tropical cyclones can reach higher atmospheric levels, reducing stability near the tropopause (Zhan and Wang, 2012; Baray et al., 1999). A lower tropopause height and a less stable lower stratosphere can facilitate deeper stratospheric intrusions, extending down to approximately 300 hPa, which have a more pronounced impact on surface cyclogenesis (Ferrara et al., 2017; Moon and Kieu, 2017; Barnes et al., 2022). These intrusions promote warm advection from the lower stratosphere and adiabatic heating of descending air, contributing to the development of an upper-level warm core and enhancing the cyclonic circulation (Ohno and Satoh, 2015; Moon and Kieu, 2017).

Prior studies have applied the Lorenz Energy Cycle (LEC) and allied limited-area energetics to diagnose cyclone development across basins (e.g., Brennan and Vincent, 1980; Smith, 1980; Michaelides, 1987, 1992; Bulic, 2006; Pezza et al., 2010). Analyses of explosive cyclogenesis across major oceanic basins indicate that environmental energetics can serve as a proxy for intense cyclone development (Black and Pezza, 2013). For subtropical systems, available studies highlight the relative importance of mixed barotropic–baroclinic conversions in their development (Dias Pinto et al., 2013; Pezza et al., 2014; Cavicchia et al., 2018), whereas extratropical systems are generally more reliant on baroclinic conversions (Dias Pinto and Rocha, 2011; Black and Pezza, 2013). There is also evidence that baroclinic influences on the LEC may inhibit tropical transition (Dias Pinto et al., 2013), while barotropic conversions tend to dominate during the tropical phases of transitioned systems (Veiga et al., 2008). However, for tropical cyclones, the literature on LEC energetics remains limited.

In parallel, vorticity and heat budgets are widely used diagnostics for investigating tropical cyclone development. Case studies of vorticity budgets indicate bottom-up initial development driven by low-level mass convergence (Montgomery et al., 2010; Wu et al., 2022). Surface latent heat fluxes near the cyclone core destabilize the atmospheric column (Fang et al., 2019; Vannière et al., 2020), while vertical vorticity advection transports vorticity upward (DesRosiers et al., 2022; Wu et al., 2022).

This upward flux strengthens boundary-layer mass convergence and can trigger rapid intensification (Raymond and López Carrillo, 2011). Nevertheless, few studies have examined these budgets for cyclones in the South Atlantic region (e.g., Dutra et al., 2017; Silva et al., 2022).

Until Hurricane Catarina in March 2004, there were no recorded instances of tropical cyclones in the South Atlantic basin (Pezza and Simmonds, 2005). Catarina originated as an extratropical cyclone that underwent tropical transition before making landfall in Southern Brazil. Although its development occurred over relatively cool sea surface temperatures, a unique combination of extreme blocking conditions, low vertical wind shear, and vigorous heat fluxes — driven by a strong air-sea thermal contrast — allowed it to intensify into a Category 1 hurricane (McTaggart-Cowan et al., 2006; Pezza et al., 2009; Vianna et al., 2010; Pereira Filho et al., 2010). More recently, in March 2019, the first documented instance of pure tropical cyclogenesis in the South Atlantic occurred near northeastern Brazil (Reboita et al., 2021). This event was influenced by anomalously warm sea surface temperatures and a blocking pattern over the South Atlantic, which reduced vertical wind shear and enabled the formation and maintenance of a tropical warm-core structure.

In February 2024, the third recorded tropical cyclone in the South Atlantic was detected by the Brazilian Navy. The cyclone, named Akará, initially developed as a subtropical system and underwent tropical transition, exhibiting a deep warm core and an eye-like feature during its mature stage (Reboita et al., 2024). While Reboita et al. (2024) provided an assessment of the synoptic conditions and physical mechanisms associated with Akará's cyclogenesis and subsequent development, further exploration is needed, particularly regarding its dynamical, thermodynamical, and energetic processes. Given the rarity of tropical transitioning systems in the South Atlantic, a comprehensive investigation of their development is essential to improve our understanding of the mechanisms driving their formation. In this context, comprehensive cyclone-centered diagnostics that jointly evaluate energetics via the Lorenz Energy Cycle together with heat and vorticity budgets remain scarce for the South Atlantic. Here, we adopt a semi-Lagrangian, storm-centered framework that integrates the LEC with phase-averaged heat and vorticity budgets to provide a unified, process-based quantification of system development. Additionally, such studies are crucial for assessing the potential impacts of climate change on their frequency and for addressing operational challenges related to their forecasting.

## 2 Data and Methods

### 2.1 Data

For the dynamic and thermodynamic analysis performed in the current study we used the European Center for Medium-Range Weather Forecasts (ECMWF) fifth generation reanalysis, the ERA5 (Hersbach et al., 2020). It offers global coverage at a horizontal spacing of  $0.25^\circ$ , with 137 vertical levels from 1000 hPa to 1 hPa. This dataset is produced using the Integrated Forecasting System (IFS) Cy41r2, which assimilates a multitude of observations, satellite and in-situ measurements, aiming

159 to provide the most accurate representation of the atmosphere currently available  
160 (Hersbach et al., 2020).

161 Additionally, we utilized data from the Geostationary Operational Environmental Satellite (GOES)-16, specifically its Channel 13, part of the Advanced Baseline  
162 Imager (Schmit et al., 2017). Channel 13 operates in the longwave infrared spectrum,  
163 centered at 10.3  $\mu\text{m}$ , with a spectral bandwidth of 0.5  $\mu\text{m}$ . The spatial resolution  
164 of Channel 13 is 2 km at the nadir, and it provides high-frequency temporal data,  
165 with imagery available every 10 minutes over the full disk and can be downloaded at  
166 <https://ftp1.cptec.inpe.br/goes16/retangular/>.

## 168 2.2 Analysis

### 169 2.2.1 Lorenz Energy Cycle Computation

170 In this study, the Lorenz Energy Cycle (LEC) was employed as a diagnostic tool  
171 to understand the energy flow within the atmosphere by decomposing atmospheric  
172 kinetic energy and available potential energy (APE) into zonal-mean and eddy com-  
173 ponents (Lorenz, 1967). The computation of the LEC was performed using the  
174 LorenzCycleToolKit (de Souza et al., 2024). The energy budget equations for the zonal  
175 and eddy forms of APE and kinetic energy are based on the formulations by Muench  
176 (1965) and Brennan and Vincent (1980), expressed as:

$$\frac{\partial A_Z}{\partial t} = BA_Z - C_Z - C_A + RG_Z \quad (1)$$

$$\frac{\partial A_E}{\partial t} = BA_E - C_E + C_A + RG_E \quad (2)$$

$$\frac{\partial K_Z}{\partial t} = BK_Z + C_Z - C_K + RK_Z \quad (3)$$

$$\frac{\partial K_E}{\partial t} = BK_E + C_E + C_K + RK_E \quad (4)$$

177 where the residual terms are defined as:

$$RK_Z = B\Phi_Z - D_Z + \epsilon_{KZ} \quad (5)$$

$$RK_E = B\Phi_E - D_E + \epsilon_{KE} \quad (6)$$

$$RG_Z = G_Z + \epsilon_{GZ} \quad (7)$$

$$RG_E = G_E + \epsilon_{GE} \quad (8)$$

178 In these equations,  $A_Z$  and  $A_E$  represent the zonal and eddy components of APE,  
179 respectively, while  $K_Z$  and  $K_E$  represent the zonal and eddy components of kinetic  
180 energy. The term  $C_Z$  describes the conversion from  $A_Z$  to  $K_Z$ , where positive values  
181 indicate ascending motion of air in warm latitudes and/or descending motion of air in  
182 cold latitudes. The term  $C_A$  describes the conversion between  $A_Z$  and  $A_E$ , where pos-  
183 itive values reflect meridional and/or vertical heat transport from relatively warmer

to colder latitudes. The term  $C_E$  denotes the conversion from  $A_E$  to  $K_E$ , with a similar interpretation to  $C_Z$ , but involving ascending (descending) motion over warmer (colder) longitudes.  $A_Z \rightarrow A_E \rightarrow K_E$  is usually referred as the baroclinic chain. Meanwhile, the term  $C_K$  is the barotropic conversion term, with positive values representing the exchange of kinetic energy between large-scale eddies ( $K_E$ ) and the zonal flow ( $K_Z$ ), such as jet streams.

$G_Z$  and  $G_E$  represent the generation of  $A_Z$  and  $A_E$ , respectively. The generation of APE is driven by diabatic heating at warmer latitudes and/or diabatic cooling at colder latitudes for  $G_Z$ , whereas for  $G_E$ , the process involves warmer and colder longitudes. The dissipation terms,  $D_Z$  and  $D_E$ , denote the loss of  $K_Z$  and  $K_E$  due to frictional processes, including surface drag and internal turbulence. The boundary flux terms include  $BA_Z$ ,  $BA_E$ ,  $BK_Z$ , and  $BK_E$ , which represent the fluxes of  $A_Z$ ,  $A_E$ ,  $K_Z$ , and  $K_E$  across the limited domain boundaries, respectively. The terms  $B\Phi_Z$  and  $B\Phi_E$  correspond to the boundary work pressure for the zonal and eddy components. However, as noted by Muench (1965), the physical interpretation of  $B\Phi_Z$  and  $B\Phi_E$  is challenging. Lastly, the  $\epsilon$  terms account for numerical errors introduced during the computation procedures.

The complete framework of the LEC, with arrows indicating positive energy fluxes, is presented in Figure 1. Although we computed the generation residual terms ( $RG_Z$  and  $RG_E$ ) and used them to estimate the  $A_Z$  and  $A_E$  budgets, direct computations of the actual  $G_E$  and  $G_Z$  terms were also performed. Since the residual terms inherently include numerical errors and subgrid-scale effects, the analysis focuses on the actual generation terms ( $G_E$  and  $G_Z$ ) to allow for a more physically meaningful interpretation. The complete mathematical expressions, including the eddy-mean decomposition, the treatment of lateral fluxes and pressure-work terms, and an extended methodological discussion are provided (de Souza et al., 2025).

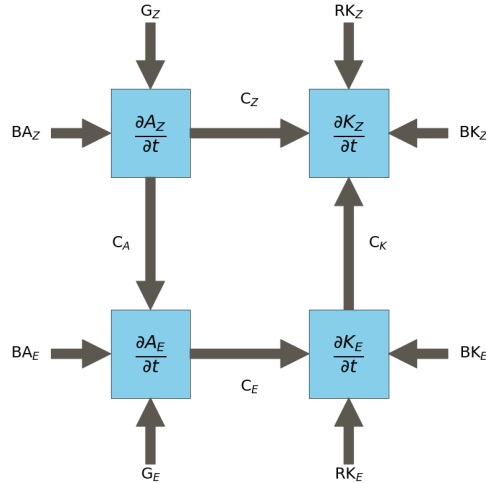


**Fig. 1** Representation of the Lorenz Energy Cycle (LEC), with arrows denoting positive energy fluxes.

210 Here, we employed a Semi-Lagrangian framework (Michaelides et al., 1999) with a  
 211  $5^\circ \times 5^\circ$  computational domain centered on the cyclone's central position at each time  
 212 step. This choice of computational domain is consistent with the typical scale of South  
 213 Atlantic subtropical cyclones, whose radii are generally near 500 km (Gozzo et al.,  
 214 2014) and it resolves the mesoscale structure of the subtropical/tropical cyclone while  
 215 minimizing the influence of unrelated circulations in the surrounding environment.  
 216 For instance, the cyclogenesis occurred in a frontal zone near the continent, close to  
 217 the South Atlantic Subtropical High (SASH) and a post-frontal migratory anticyclone  
 218 (Reboita et al., 2024). The chosen domain therefore encompassed the cyclone core  
 219 while excluding, as far as possible, the direct influence of these neighboring systems, in  
 220 line with the primary objective of isolating the energetics associated with the cyclone  
 221 itself.

## 222 2.2.2 Heat and Vorticity Budgets

223 The heat and vorticity budgets were employed as diagnostic tools in this study, with  
 224 the calculations performed using the ATMOS-BUD program (de Souza et al., 2025).  
 225 These analyses provide a deeper understanding of the dynamical and thermodynam-  
 226 ical processes contributing to the intensification of cyclonic circulation, as well as the  
 227 three-dimensional structure of the cyclone and its interactions with the surrounding  
 228 environment (e.g., Dutra et al., 2017).

229 The heat budget is described by the thermodynamic equation:

$$\underbrace{\frac{\partial T}{\partial t}}_{(A)} = \underbrace{-\mathbf{V}_h \cdot \nabla_h T}_{(B)} - \underbrace{S_p \omega}_{(C)} + \underbrace{Q}_{(D)}, \quad (9)$$

230 where  $T$  is the temperature [ $K$ ],  $t$  is the time [ $s$ ],  $\mathbf{V}_h$  is the horizontal wind vector  
 231 [ $m s^{-1}$ ],  $\nabla_h$  is the horizontal gradient operator  $\omega$  is the vertical velocity in pressure  
 232 coordinates [ $Pa s^{-1}$ ], and  $Q$  is the diabatic heating rate [ $K s^{-1}$ ].  $S_p$  is the static  
 233 stability term, approximated by:

$$S_p = \frac{RT}{c_p p} - \frac{\partial T}{\partial p} = -\frac{T}{\theta} \frac{\partial \theta}{\partial p}, \quad (10)$$

234 where  $R$  is the specific gas constant for dry air [ $287.05 J kg^{-1} K^{-1}$ ],  $c_p$  is the  
 235 specific heat capacity at constant pressure [ $1004 J kg^{-1} K^{-1}$ ],  $p$  is the pressure [Pa],  
 236 and  $\theta$  is the potential temperature [ $K$ ].

237 In the thermodynamic equation, term (A) represents the local tendency of temper-  
 238 ature, term (B) represents horizontal temperature advection by the horizontal wind  
 239 components, term (C) accounts for the total vertical motion weighted by the static  
 240 stability term  $S_p$ , indicating vertical advection in addition to adiabatic expansion/-  
 241 compression, and term (D) represents diabatic heating, including contributions from  
 242 latent heat release, radiative heating, or cooling, and subgrid scale processes. The  
 243 diabatic heating term was computed as a residual, obtained by subtracting the con-  
 244 tributions of all other terms on the right-hand side from the local tendency term. As  
 245 such, this term also include numerical errors and therefore should be examined with  
 246 caution.

247 The vorticity budget is expressed as:

$$\underbrace{\frac{\partial \zeta}{\partial t}}_{(A)} = \underbrace{-\mathbf{V}_h \cdot \nabla_h \zeta}_{(B)} - \underbrace{\omega \frac{\partial \zeta}{\partial p}}_{(C)} - \underbrace{\beta v}_{(D)} - \underbrace{\zeta \nabla_h \cdot \mathbf{V}_h}_{(E)} - \underbrace{f \nabla_h \cdot \mathbf{V}_h}_{(F)} + \underbrace{\left( \frac{\partial \omega}{\partial y} \frac{\partial u}{\partial p} - \frac{\partial \omega}{\partial x} \frac{\partial v}{\partial p} \right)}_{(G)} + \underbrace{F_\zeta}_{(H)} \quad (11)$$

248 where  $\zeta$  is the relative vorticity [ $s^{-1}$ ],  $\beta$  is the meridional gradient of the Coriolis  
249 parameter [ $m^{-1}s^{-1}$ ],  $v$  is the meridional wind component [ $m s^{-1}$ ],  $f$  is the Coriolis  
250 parameter [ $s^{-1}$ ],  $u$  and  $v$  are the zonal and meridional wind components [ $m s^{-1}$ ].

251 In the vorticity equation, term (A) represents the local tendency of vorticity,  
252 while term (B) corresponds to the horizontal advection of relative vorticity. Term (C)  
253 accounts for the vertical advection of relative vorticity, and term (D) represents the  
254 advection of planetary vorticity. Term (E) describes the contribution of relative vor-  
255 ticity to stretching caused by horizontal convergence or divergence (stretching term,  
256 ZD), whereas term (F) represents the planetary vorticity contribution to the stretch-  
257 ing term (FD). Term (G) captures the tilting of horizontal vorticity into the vertical  
258 due to vertical wind shear. Finally, term (H) is the friction term and subgrid scale  
259 contributions ( $F_\zeta$ ), computed as a residual, defined as the difference between the local  
260 tendency (A) and the sum of all other terms on the right-hand side. This residual  
261 term also accounts for any unrepresented processes and numerical errors. As noted in  
262 previous studies (Reed and Johnson, 1974; Chu et al., 1981, e.g.), regions with sig-  
263 nificant convective activity often exhibit an apparent source of cyclonic vorticity in  
264 the upper troposphere and a sink near the surface, suggesting vertical transport of  
265 vorticity by convective processes.

266 Similarly as for the LEC analysis, for both heat and vorticity budgets, a  $5^\circ \times 5^\circ$   
267 computational domain centered on the cyclone's central position was employed at  
268 each time step. The terms were then spatially averaged to facilitate the analysis.

### 269 2.2.3 Cyclone Phase Space

270 The Cyclone Phase Space (CPS) framework was utilized in this study to classify  
271 cyclones into extratropical, subtropical, and tropical categories, as well as to identify  
272 transitions between these types (Hart, 2003). The CPS is a diagnostic tool based on  
273 three key parameters derived from geopotential height fields: the lower-tropospheric  
274 thermal asymmetry ( $B$ ), the thermal wind in the upper troposphere ( $V_T^U$ ), and the  
275 thermal wind in the lower troposphere ( $V_T^L$ ). These parameters are computed from  
276 vertical and horizontal temperature gradients, providing a robust representation of  
277 the cyclone's structure.

278 The parameter  $B$  is defined as:

$$B = h \left[ \left( \overline{Z}_{600 \text{ hPa}} - \overline{Z}_{900 \text{ hPa}} \right)_R - \left( \overline{Z}_{600 \text{ hPa}} - \overline{Z}_{900 \text{ hPa}} \right)_L \right]_{500 \text{ km}}, \quad (12)$$

279 where  $Z$  represents geopotential height, and  $R$  and  $L$  denote the right and left  
280 sides of the storm's motion. The overbar indicates the areal mean over a semicircle

281 with a radius of 500 km. The term  $h$  is set to +1 for the Northern Hemisphere and  
282 -1 for the Southern Hemisphere, ensuring consistency in calculations.

283 The thermal winds at lower and upper levels are calculated as the vertical  
284 derivative of the horizontal geopotential height gradient, expressed as:

$$285 \quad -|V_T^L| = \frac{\delta (Z_{\max} - Z_{\min})_{500 \text{ km}}}{\delta \ln p}, \quad \text{for levels 900 to 600 hPa}, \quad (13)$$

$$-|V_T^U| = \frac{\delta (Z_{\max} - Z_{\min})_{500 \text{ km}}}{\delta \ln p}, \quad \text{for levels 600 to 300 hPa}. \quad (14)$$

286 Cyclone classification is based on the position of the system within the phase space:  
287 tropical cyclones are characterized by symmetric warm cores, extratropical cyclones by  
288 asymmetric cold cores, and subtropical cyclones exhibit intermediate characteristics  
289 (Hart, 2003). The classification criteria are as follows (Wood et al., 2023): systems are  
290 classified as extratropical when  $B \gg 10 \text{ m}$ ,  $-|V_T^L| < 0$ , and  $-|V_T^U| < 0$ ; tropical when  
291  $B < 10 \text{ m}$ ,  $-|V_T^L| > 0$ , and  $-|V_T^U| > 0$ . For subtropical cyclones over the South Atlantic  
292 Ocean, the thresholds are  $-25 < B < 25 \text{ m}$ ,  $-|V_T^L| > -50$ , and  $-|V_T^U| < -10$  (Gozzo  
293 et al., 2014, 2017; de Jesus et al., 2022; Cardoso et al., 2022).

### 294 2.3 Cyclone Tracking and Phase Detection

295 To detect the cyclone's central position and identify the phases of cyclogenesis and  
296 cyclolysis, we employed a semi-supervised method. This approach utilized distinct  
297 variables, including mean sea level pressure (MSLP), relative vorticity at 850 hPa  
298 ( $\zeta_{850}$ ), and potential vorticity (PV) at the same vertical level. The  $\zeta_{850}$  and PV fields  
299 were computed using the Python open-source library MetPy (May et al., 2022). The  
300 decision to use  $\zeta_{850}$  was motivated by its superior capability to capture the early  
301 development stages of cyclones, particularly within the latitude range of 20°S to 40°S.  
302 In this region, strong pressure gradients often prevent cyclones from exhibiting a closed  
303 isobar until later stages of their development (Sinclair, 1994; Hoskins and Hodges,  
304 2002; Gramcianinov et al., 2019).

305 The initial stages of cyclone development were identified by visually locating cen-  
306 ters of cyclonic  $\zeta_{850}$  associated with regions of low MSLP. A program was then  
307 employed to detect and refine the cyclone center's position. The PV field proved  
308 instrumental in distinguishing  $\zeta_{850}$  signals arising from strong wind shear from those  
309 corresponding to actual cyclone development. An initial *first-guess* position was placed  
310 near the cyclonic  $\zeta_{850}$  feature, and the program automatically adjusted this position by  
311 searching for the MSLP minimum within a  $1^\circ \times 1^\circ$  square surrounding the initial esti-  
312 mate. Once the first closed isobar was detected, the *first-guess* position was relocated  
313 near its center, and the program further refined the location to align with the actual  
314 MSLP minimum. Cyclolysis was defined as the time at which a closed isobar could no  
315 longer be identified in the synoptic chart. The resulting track from this methodology  
316 closely aligned with that of Reboita et al. (2024). However, our approach enabled an  
317 earlier detection of cyclogenesis, providing valuable insights into the dynamical and  
318 thermodynamical mechanisms driving cyclone development.

319 In addition to distinguishing the cyclone between subtropical and tropical stages,  
320 we utilized the Cyclophaser program to separate the system into incipient, intensifi-  
321 cation, mature, and decay phases (de Souza et al., 2025). The Cyclophaser uses the  
322 system's central  $\zeta_{850}$  and its derivative to detect distinct life cycle phases. A pre-  
323 processing step filters the  $\zeta_{850}$  series, removing spurious oscillations and those related  
324 to small-scale features. The filtered series is then smoothed to represent a sinusoidal  
325 pattern. For the Southern Hemisphere, the intensification (decay) phase is detected  
326 between vorticity peaks (valleys) and subsequent valleys (peaks). The mature phase  
327 is identified near the vorticity valleys using specific thresholds based on its derivative,  
328 while the incipient stage is defined as the period between cyclogenesis and the onset  
329 of intensification. For further details on the method, refer to de Souza et al. (2024)  
330 and de Souza et al. (2025). Synoptic charts are presented in the subsequent sections  
331 for each distinct phase, under the assumption that these phases represent relatively  
332 homogeneous dynamic and thermodynamic processes (e.g., de Souza et al., 2024).  
333 Additionally, heat and vorticity budget results, as well as energy terms, are averaged  
334 over each phase based on this same assumption, as in Dutra et al. (2017).

### 335 3 Results

336 Figure 2 shows the cyclone track, while Figure 3 illustrates the phases of Akará's  
337 life cycle, identified through its central  $\zeta_{850}$ . The classification of these phases is  
338 further corroborated by the central mean sea level pressure (MSLP). The periods  
339 during which the cyclone was classified as subtropical or tropical are also indicated in  
340 Figure 3. Complementarily, Figure 3 presents the zonal anomaly of the cyclone's core  
341 temperature, following the methodology of Reboita et al. (2021) and Reboita et al.  
342 (2024). Here, we mark system genesis at 12Z on February 14, rather than the 12Z  
343 on February 15 definition in Reboita et al. (2024) (see Section 3.1), and define the  
344 tropical phase as spanning 06Z on February 17 to 06Z on February 21, following the  
345 authors' classification. A detailed discussion of Akará's transition from a subtropical  
346 to a tropical cyclone, linking these classifications to synoptic conditions in the region,  
347 has already been provided by Reboita et al. (2024) and is not revisited here. Instead,  
348 this study focuses on the dynamic and thermodynamic processes that governed the  
349 cyclone's evolution throughout its life cycle.

#### 350 3.1 Incipient Stage

351 An advantage of utilizing relative vorticity, in addition to sea level pressure, for cyclone  
352 tracking is the ability to identify cyclogenesis before a closed isobar appears on surface  
353 charts (e.g., Sinclair, 1994; Gramcianinov et al., 2019). As demonstrated in de Souza  
354 et al. (2024), neglecting this early detection of the cyclone's incipient stage would result  
355 in the South Atlantic tracks being displaced eastward, farther from the continent. For  
356 instance, while Reboita et al. (2024) identified cyclogenesis at 12Z on February 15,  
357 in this study, it is detected earlier, at 21Z on February 14, during a period termed  
358 "Pre-cyclogenesis" by the authors.

359 As highlighted by Reboita et al. (2024), cyclogenesis coincided with the passage of  
360 a cold front near Southeastern Brazil. On the beginning of the incipient stage, although

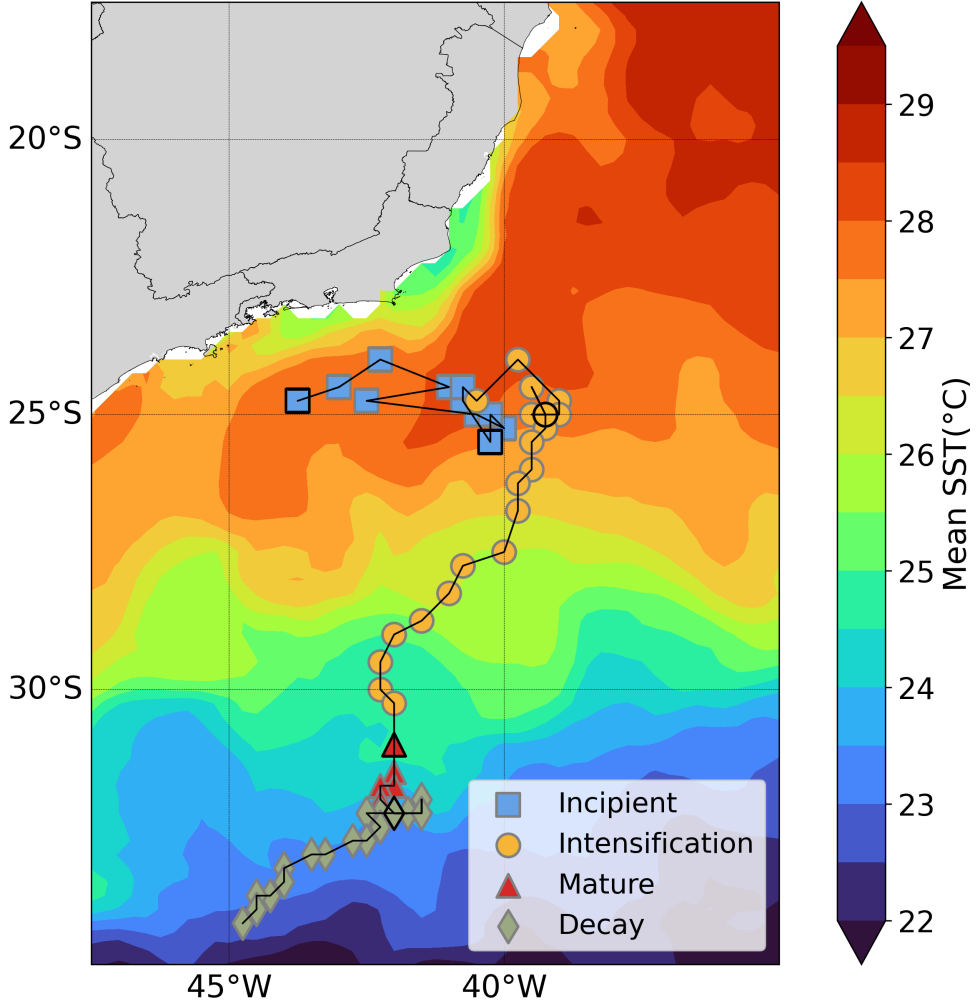


**Fig. 2** Cyclone track and sea surface temperature (SST), expressed in  $^{\circ}\text{C}$ , averaged over the cyclone's duration from February 14 at 21Z to February 22 at 21Z. The track marker are color-coded to represent distinct phases of the cyclone's lifecycle. More opaque markers with darker contours indicate the dates corresponding to the snapshots shown in Figures 5, 6, 11, 12, 13 and 14.

the CPS indicates a symmetric deep cold core (Figure 4), the zonal temperature anomaly reveals an initially warm mid-upper troposphere (Figure 3), attributable to deep convection in the frontal region near the cyclone center, between  $50^{\circ}\text{W}$  and  $40^{\circ}\text{W}$  and around  $25^{\circ}\text{S}$ , as evidenced by brightness temperatures as low as  $-60^{\circ}\text{C}$  (Figure 5a). During its genesis, the system is located in a region characterized by strong thermal contrasts between the ocean and the atmosphere, between two low-pressure systems along the frontal zone (Figure 5b). Southeast of the cyclone center, near  $37^{\circ}\text{S}$ , a cutoff low is evident in the 500 hPa geopotential height field (Figure 5c).

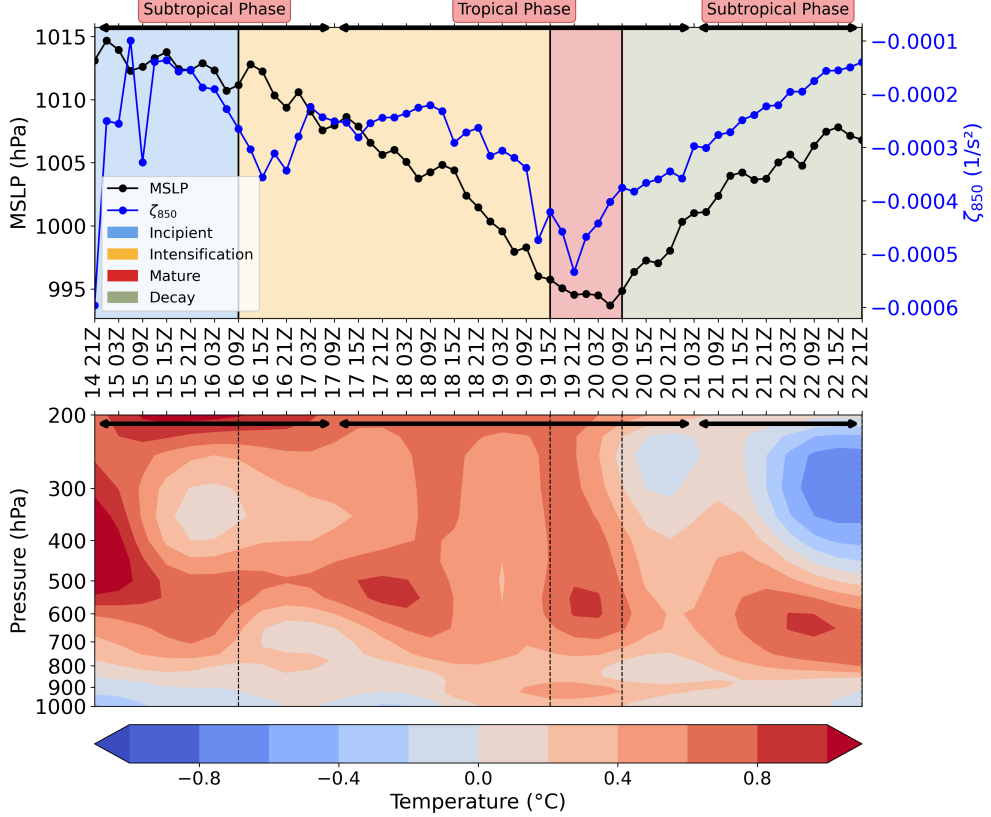


**Fig. 3** (Top) Time series of mean sea level pressure (MSLP, black line) and relative vorticity at 850 hPa ( $\zeta_{850}$ , blue line) at the cyclone center, as identified by the Cyclophaser program. Shaded areas represent the different phases of the cyclone's life cycle (incipient, intensification, mature, and decay), while the horizontal arrows indicate the subtropical and tropical phases. (Bottom) Vertical cross-section of the temperature deviation ( $^{\circ}\text{C}$ ) near the cyclone center throughout the cyclone's life cycle. The deviation is obtained by subtracting the mean temperature in a  $2^{\circ} \times 10^{\circ}$  box from that in a  $2^{\circ} \times 30^{\circ}$  box, both centered on Akará's center. Dashed vertical lines indicate phase transitions: incipient to intensification, intensification to mature, and mature to decay. The horizontal arrows similarly indicate the subtropical and tropical phases.

369 On February 15, a cutoff low begins to approach the surface cyclone (Figure 6c),  
 370 which subsequently moves southeastward. This interaction explains the relatively cold  
 371 core observed in the mid-upper troposphere in Figure 3. The presence of a cutoff low at  
 372 mid-upper levels is recognized as one of the primary mechanisms driving subtropical  
 373 cyclogenesis (da Rocha et al., 2019). During this phase, the cyclone's thermal structure  
 374 evolves toward a warmer, more symmetric state, as indicated by the CPS (Figure 4).  
 375 Specifically, the  $B$  term decreases steadily to negative values, while both  $-|V_T^L|$  and  
 376  $-|V_T^U|$  increase in magnitude, indicating a shallow symmetric warm core. Additionally,  
 377 the tropopause near the cyclone center becomes shallower, as evidenced by the upward  
 378 displacement of the  $-2$  PVU surface in Figure 6c.

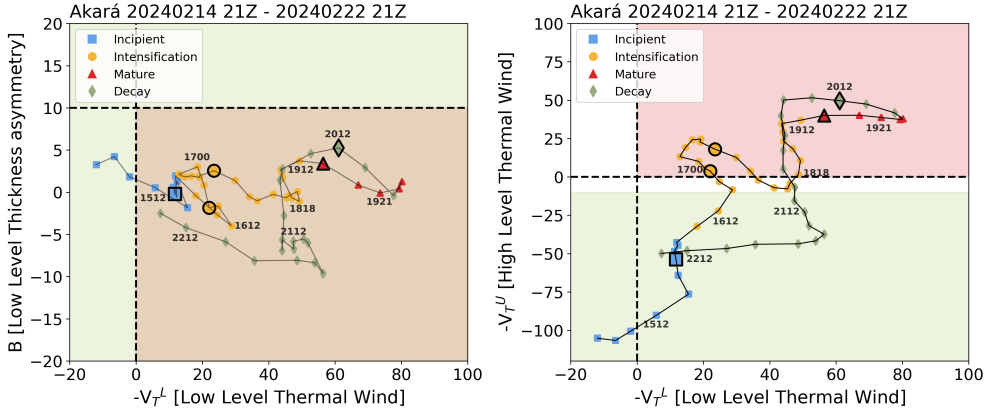


**Fig. 4** Cyclone Phase Space (CPS) diagram for the Akará tropical transition from February 14 to February 22, 2024. (a) Low-level thickness asymmetry ( $B$ ) and lower-tropospheric thermal wind ( $-V_T^L$ ), (b) upper-tropospheric thermal wind ( $-V_T^U$ ) and lower-tropospheric thermal wind ( $-V_T^L$ ). Markers indicate distinct lifecycle phases, with annotations representing dates in day-hour format and enlarged markers indicate the dates corresponding to the snapshots shown in 5, 6, 11, 12, 13 and 14. The background shading corresponds to phase classification thresholds for subtropical (based on Southern Atlantic criteria) and tropical cyclones.

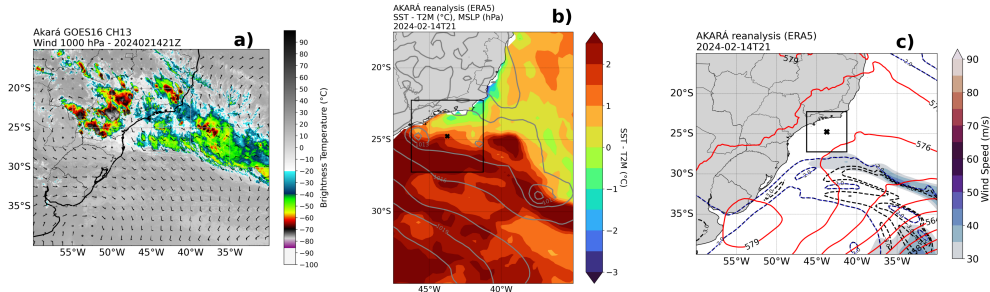


**Fig. 5** Synoptic conditions at 21Z on 14 February 2024, during the early-intensification stage of the system.. (a) Brightness temperature from GOES-16 Channel 13 (shading, in  $^{\circ}\text{C}$ ) and wind vectors at 1000 hPa. (b) Difference between sea surface temperature and 2-meter air temperature (SST – T2M; shading, in  $^{\circ}\text{C}$ ) and mean sea level pressure (contours, in hPa). (c) Geopotential height at 500 hPa (red contours, in dam), wind speed at 200 hPa (shading, in  $\text{m s}^{-1}$ ), and potential vorticity at 200 hPa (dashed contours, in PVU). Black contours represent the -3 and -4 PVU levels, while the blue contour corresponds to the -2 PVU level. Black contours represent the -3 and -4 PVU levels, while the blue contour corresponds to the -2 PVU level. The black cross denotes the cyclone center. The black rectangles indicate the analysis domain used for the Lorenz Energy Cycle (LEC), heat budget, and vorticity budget diagnostics.

379 During the incipient phase (Figure 3), the cyclone was located over relatively warm  
 380 waters, with sea surface temperatures exceeding  $28^{\circ}\text{C}$  (Figure 2). Simultaneously,  
 381 a thermal contrast of up to  $3^{\circ}\text{C}$  between the ocean and the atmosphere near the  
 382 cyclone center (Figure 5b and 6b) enhanced latent and sensible heat fluxes to the lower

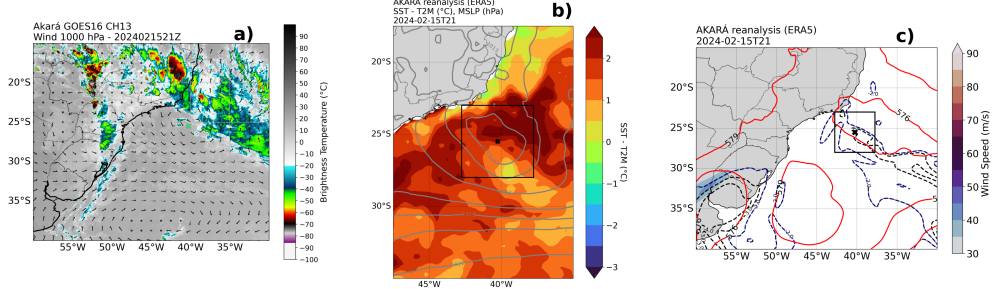


**Fig. 6** Synoptic conditions at 21Z on 15 February 2024, during the mid-incipient stage of the system. (a) Brightness temperature from GOES-16 Channel 13 (shading, in  $^{\circ}\text{C}$ ) and wind vectors at 1000 hPa. (b) Difference between sea surface temperature and 2-meter air temperature ( $\text{SST} - \text{T2M}$ ; shading, in  $^{\circ}\text{C}$ ) and mean sea level pressure (contours, in hPa). (c) Geopotential height at 500 hPa (red contours, in dam), wind speed at 200 hPa (shading, in  $\text{m s}^{-1}$ ), and potential vorticity at 200 hPa (dashed contours, in PVU). The black cross denotes the cyclone center. The black rectangles indicate the analysis domain used for the Lorenz Energy Cycle (LEC), heat budget, and vorticity budget diagnostics.

383 atmosphere. These fluxes reduced boundary layer stability (e.g., Pezzi et al., 2009,  
 384 2021), thereby promoting convective activity. Independently, the vertical structure  
 385 of horizontal vorticity advection exhibits increasing cyclonic advection with height  
 386 (Figure 7a), which, by the quasi-geostrophic omega equation, supports upward motion  
 387 (Trenberth, 1978; Maddox and Doswell III, 1982).

388 Additionally, the positive  $G_E$  term (Figure 8a) and the diabatic heating term  
 389 (Figure 9a) indicate significant latent heat release associated with enhanced con-  
 390 vective activity. While Reboita et al. (2024) suggested that warm advection by the  
 391 South Atlantic Subtropical High (SASH) supported the cyclone's initial development,  
 392 our analysis indicates that this contribution was negligible compared to other ther-  
 393 modynamic processes. Instead, diabatic heating was the primary contributors for  
 394 heating the troposphere and, consequently, deepening the surface pressure. Meanwhile,  
 395 adiabatic expansion due to the convective activity acted in the opposite direction,  
 396 contributing for cooling the troposphere.

397 The vorticity budget indicates a cyclonic tendency across all vertical levels during  
 398 the incipient phase (Figure 7a). Near the surface, the primary contributor to cyclonic  
 399 vorticity is the relative vorticity component of the stretching term (ZD), which is  
 400 associated with mass convergence. Between 900 hPa and 350 hPa, vertical advection  
 401 emerges as the main contributor to the negative tendency, while above this layer,  
 402 horizontal advection dominates. Throughout much of the lower and middle tropo-  
 403 sphere, vertical advection is largely canceled by the tilting term, a behavior similar to  
 404 that observed for the South Atlantic subtropical cyclone Anita (Dutra et al., 2017).  
 405 Above 200 hPa, the planetary vorticity contribution to the stretching term (FD) sur-  
 406 passes ZD in magnitude, reflecting mass divergence. Although small in magnitude,  
 407 the negative values of planetary vorticity advection throughout most of the atmo-  
 408 spheric column indicate that the predominant meridional flow during this phase was  
 409 northward, influenced by the post-frontal anticyclone. The small magnitude of the

tilting term is associated with the weak wind shear in the Akará's environment, as demonstrated by Reboita et al. (2024).

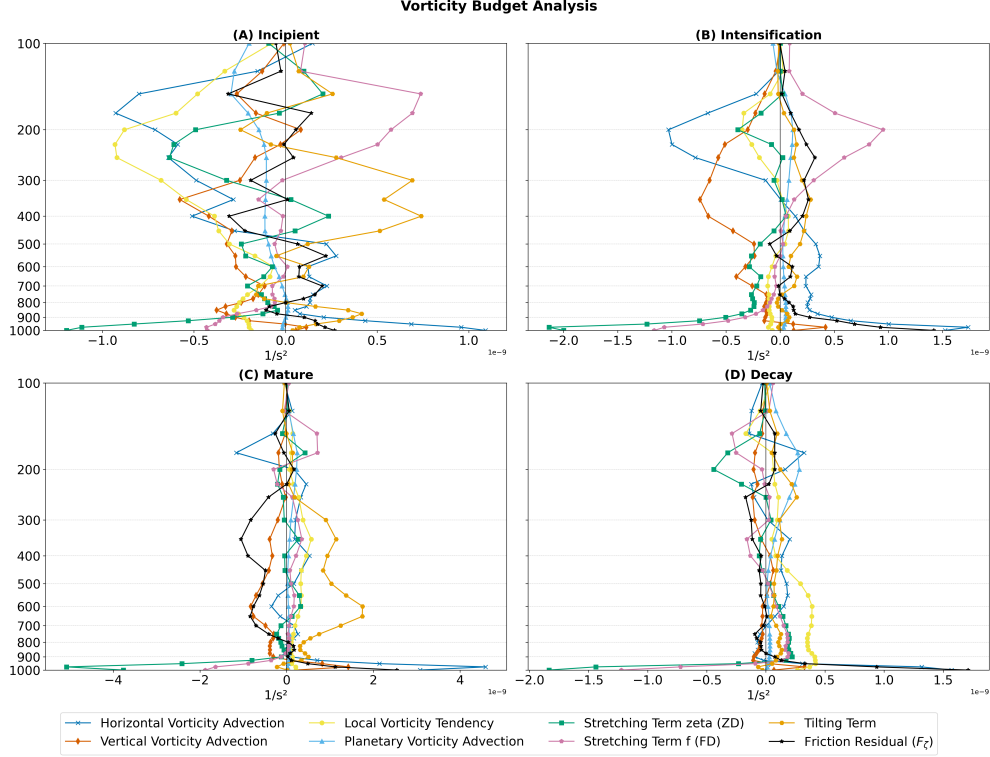


**Fig. 7** Vertical profiles of the vorticity budget terms during the distinct phases of the Akará lifecycle: (a) Incipient, (b) Intensification, (c) Mature, and (d) Decay, expressed in  $s^{-2}$ . Values are averaged over all analysis times within each phase and spatially over the domain used to compute the budgets.

The LEC analysis for the incipient stage reveals that the barotropic conversion term  $C_K$  ( $K_Z \rightarrow K_E$ ) was the primary energy source driving cyclone (eddy) development (Figure 8a). In contrast, the baroclinic chain ( $A_Z \rightarrow A_E \rightarrow K_E$ ) exhibited modest contributions, with  $G_E$  being the dominant term supporting  $K_E$ . The low  $C_A$  values align with the limited contribution from horizontal temperature advection in the heat budget, indicating weak meridional heat transport. Meanwhile, the moderate  $G_Z$  and  $C_E$  values are associated with ascending motions (and consequent latent heat release) in the frontal region (lower latitudes) and subsidence in the post-frontal region (higher latitudes).

Thus, during the incipient phase, the weak baroclinic environment near Akará provided energy to an upper-level jet structure, associated with a through (Figure 5a), while also importing  $K_Z$  from the boundaries. Most of the  $K_Z$  was either converted into  $K_E$  or dissipated through the residual term, leading to a sharp decrease in this

component over time. These barotropic conversions were most intense in the mid-upper troposphere, especially between 300 and 400 hPa (Figure 10b). However, minor barotropic conversions occurred near the surface, related to the horizontal wind shear from the post-frontal and the SASH. Lastly, while some of the  $K_E$  was lost through the residual term or exported out of the domain via  $BK_E$ , the fluxes from both  $A_E$  and  $K_Z$  contributed to a net increase in  $K_E$  over time.

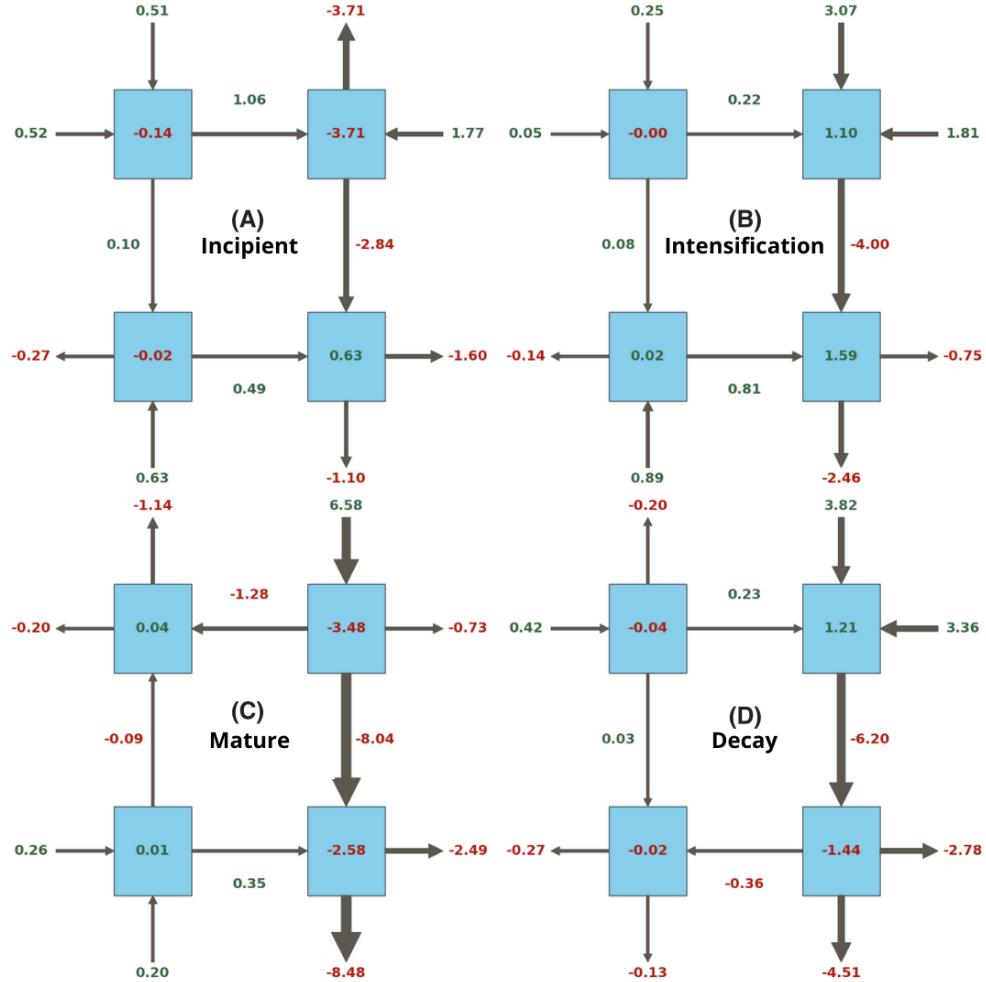


**Fig. 8** Lorenz Energy Cycle (LEC) diagrams representing the energy exchanges during each phase of the Akará lifecycle: (a) Incipient, (b) Intensification, (c) Mature, and (d) Decay. The blue boxes represent the energy reservoirs for zonal and eddy components of available potential energy (APE) and kinetic energy (KE). Arrows indicate the direction and magnitude of energy conversions between these reservoirs, with positive values in green and negative values in red, expressed in units of  $\text{W m}^{-2}$ . The terms are defined in Figure 1.

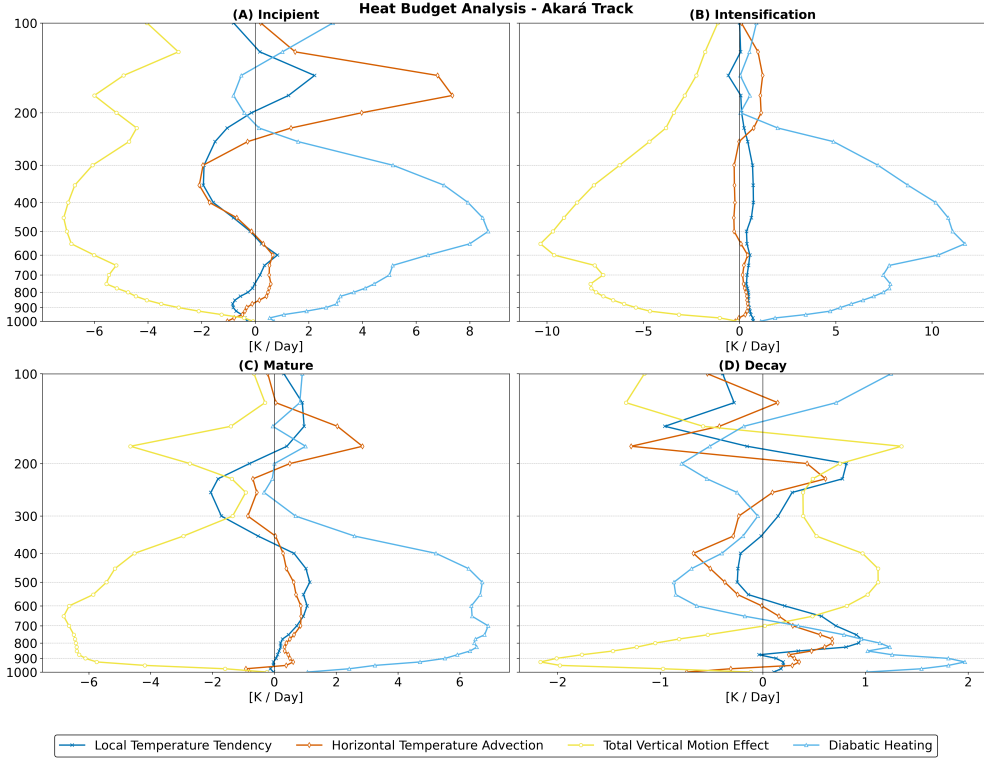


**Fig. 9** Vertical profiles of the heat budget terms during the distinct phases of the Akará lifecycle: (a) Incipient, (b) Intensification, (c) Mature, and (d) Decay, expressed in K/day. Values are averaged over all analysis times within each phase and spatially over the domain used to compute the budgets.

### 431 3.2 Intensification Stage

432 At the beginning of the intensification phase, at 09Z on February 16, the CPS already  
 433 indicates a shallow, symmetric warm core (Figure 4), and the cyclone-related cloudiness  
 434 begins to exhibit a spiral pattern (Figure 11a). This shallow warm-core feature  
 435 is also evident in the zonal mean temperature deviation field (Figure 3), where a  
 436 warm layer extends approximately between 800 and 400 hPa. Above this layer, a cold  
 437 anomaly associated with the cutoff low persists until 15Z on February 17.

438 During this period, the cyclone is located over sea surface temperatures (SSTs)  
 439 ranging from 27.5°C to 28.5°C (Figure 2), although the air-sea temperature contrast  
 440 is less pronounced (Figure 11b). Despite the weaker thermal contrast at the surface,  
 441 the vertical temperature structure, characterized by the presence of the upper-level  
 442 cold anomaly, remains favorable for convective instability, thereby enhancing upward  
 443 motion. This configuration is consistent with other subtropical systems in the region,  
 444 where upper-level forcing compensates for reduced surface-based instability (e.g.,

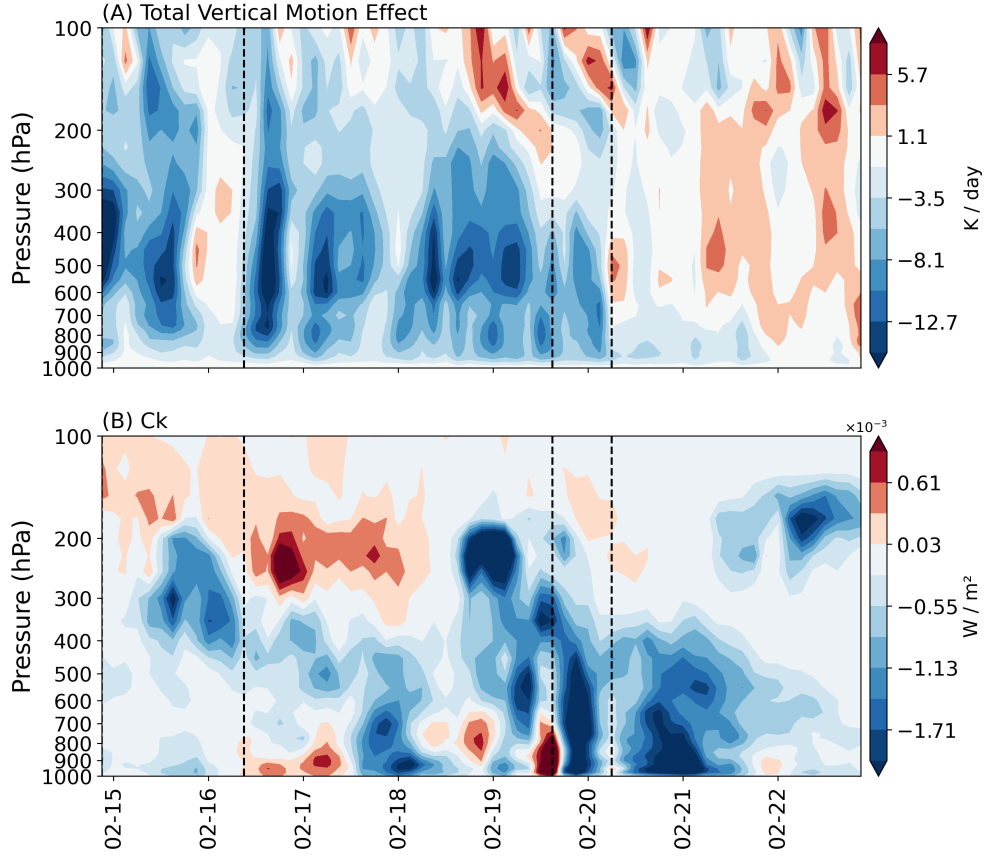


**Fig. 10** (Top) Time–pressure Hovmöller diagram of the total vertical motion effect ( $S_P \times \omega$ ) along the Akará track from February 15 to February 22, 2024, expressed in  $\text{K day}^{-1}$ , computed as spatial means over a storm-following  $5^\circ \times 5^\circ$  domain. Shading represents adiabatic cooling (blue) and warming (red) induced by vertical motion, with negative values indicating cooling due to upward motion and positive values indicating warming due to subsidence. (Bottom) Time–pressure Hovmöller diagram of the barotropic conversion term ( $C_K$ ) along the Akará track, expressed in  $\text{W m}^{-2}$ . Negative values (blue) indicate energy conversion from zonal kinetic energy ( $K_Z$ ) to eddy kinetic energy ( $K_E$ ), while positive values (red) indicate the reverse process. Dashed vertical lines mark the key phase transitions in the cyclone’s lifecycle: incipient to intensification, intensification to mature, and mature to decay. For both figures, values are averaged spatially over the domain used to compute the budgets.

445 Reboita et al., 2022). The resulting convective activity leads to an increase in the mag-  
 446 nitude of both the diabatic heating term (Figure 9b) and the  $G_E$  term (Figure 8b),  
 447 relative to the incipient stage.

448 Consequently, there is a tendency for heating throughout most of the atmospheric  
 449 column, especially in the mid-troposphere (Figure 9b). Although the total vertical  
 450 motion effect term partially counterbalances the diabatic term during the intensifica-  
 451 tion phase, the diabatic term dominates, contributing to the observed heating. This  
 452 heating on the cutoff low layer is primarily attributed to latent heat release from

453 convective activity. Meanwhile, horizontal temperature advection is negligible up to  
 454 approximately 200 hPa. Above this level, while the magnitude of this term increases,  
 455 adiabatic cooling and the vanishing diabatic term result in net cooling in the upper  
 456 troposphere, as observed in Figure 3. Lastly, from a quasi-geostrophic perspective, the  
 457 vertical derivative of the diabatic term contributes to lowering geopotential height in  
 458 a deep layer near the surface.

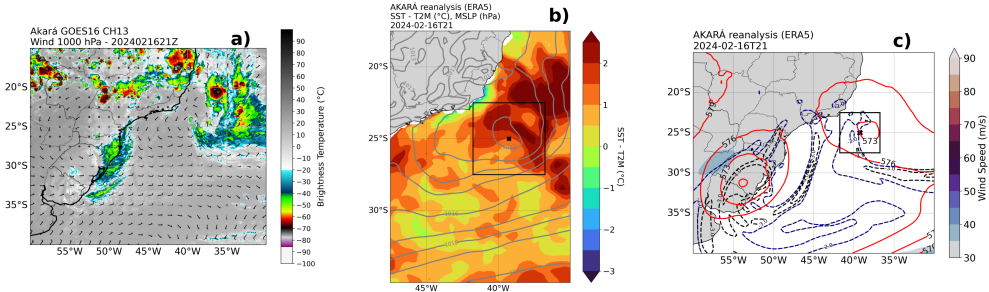


**Fig. 11** Synoptic conditions at 21Z on 16 February 2024, during the early-intensification stage of the system.. (a) Brightness temperature from GOES-16 Channel 13 (shading, in  $^{\circ}\text{C}$ ) and wind vectors at 1000 hPa. (b) Difference between sea surface temperature and 2-meter air temperature ( $\text{SST} - \text{T2M}$ ; shading, in  $^{\circ}\text{C}$ ) and mean sea level pressure (contours, in hPa). (c) Geopotential height at 500 hPa (red contours, in dam), wind speed at 200 hPa (shading, in  $\text{m s}^{-1}$ ), and potential vorticity at 200 hPa (dashed contours, in PVU). Black contours represent the  $-3$  and  $-4$  PVU levels, while the blue contour corresponds to the  $-2$  PVU level. The black cross denotes the cyclone center. The black rectangles indicate the analysis domain used for the Lorenz Energy Cycle (LEC), heat budget, and vorticity budget diagnostics.

459 Regarding the vorticity budget, the cyclonic vorticity tendency at both lower and  
 460 upper levels is smaller than during the incipient phase (Figure 7b). Near the surface,  
 461 the FD and especially the ZD terms are intense contributors to cyclonic vorticity, indi-  
 462 cating mass convergence, although they are largely offset by anticyclonic advection and  
 463 the friction term. The vertical vorticity advection increases in magnitude compared  
 464 to the incipient stage, particularly between 500 and 200 hPa, where it becomes the  
 465 primary contributor to cyclonic circulation from 900 hPa to approximately 250 hPa.  
 466 Above this level, cyclonic horizontal vorticity advection dominates and ZD indicates  
 467 mass divergence, fostering the vertical ascent. Although planetary vorticity advection  
 468 becomes positive during this phase, indicating predominantly southward flow as the  
 469 anticyclonic flow weakens, its magnitude remains negligible compared to other terms.  
 470

471 Similar to the incipient phase, the vorticity advection profile, anticyclonic near  
 472 the surface and cyclonic near 200 hPa, also favors ascent. From a quasi-geostrophic  
 473 perspective, an upper-level trough or cutoff low, as present in this case, induces down-  
 474 stream (eastward) cyclonic vorticity advection and upstream (westward) anticyclonic  
 475 advection. This dipole structure enhances ascent on the leading edge and descent on  
 476 the trailing side. Such a pattern is evident in the vertical cross-section at 21Z on 16  
 477 February (Figure S1a), where subsidence is observed west of the cyclone center and  
 ascent east of it.

478 During this phase, the cyclonic tendency observed at mid-to-upper levels con-  
479 tributes to the intensification of the mid-to-upper-level cyclonic structure, accompa-  
480 nied by a further lowering of the tropopause near the cyclone center (Figure 11c).  
481 Additionally, the tilting term is weaker than during the incipient stage as the cyclone  
482 moves southward toward the frontal region, coinciding with a decrease in vertical  
483 wind shear (Reboita et al., 2024). At this stage, Akará already exhibits a barotropic  
484 structure.

485 In addition to the cyclone's barotropic structure, its environment also becomes  
486 more barotropic during the intensification phase. This is reflected in the LEC, which  
487 shows a sharp decrease in the  $C_Z$  term and the baroclinic conversion term  $C_A$ . Con-  
488 sequently, the primary energy source for  $C_E$  is the  $G_E$  term, associated with latent  
489 heat release. At the same time, barotropic conversions increase, with  $C_K$  becoming  
490 more negative. Notably, barotropic conversions are the primary energy sources driv-  
491 ing Akará's intensification. During this phase, there is also a sharp increase in the  
492  $K_E$  budget, indicating system intensification, accompanied by a twofold increase in  
493 the  $RK_E$  term, linked to increased frictional dissipation, as indicated by the  $F_\zeta$  term  
494 (Figure 7b). The increase in the friction near the surface also helps on promoting  
495 mass convergence and therefore upward motion, due to the effect of Ekman pumping  
496 on the boundary layer (Hamouda and Kucharski, 2019, e.g.,).

497 By February 17, the entire tropospheric column becomes warm (Figure 3), mark-  
498 ing the system's tropical transition (Wood et al., 2023; Reboita et al., 2024). This  
499 transition is further confirmed by the CPS, where the  $V_T^L$  and  $V_T^U$  parameters indicate  
500 the development of a deep warm core (Figure 4b). Although diabatic heating signifi-  
501 cantly contributes to this warming, as discussed earlier in this section and by Reboita  
502 et al. (2024), an important contribution is neglected when only low-level forcing is  
503 considered, as discussed below.

504 After the tropical transition, while Akará is still over warm waters, above 27  
505 °C (Figure 2), it transitions to a relatively cooler atmospheric region than during  
506 the subtropical phase, with a higher thermal contrast between the ocean and the  
507 atmosphere (Figure 12b). At the same time, the tropopause deepens near the cyclone  
508 core, with the potential vorticity field at 200 hPa displaying values as low as -4 PVU  
509 (Figure 12c).

510 The analysis of the total vertical motion effect term (Figure 10a) indicates evidence  
511 of stratospheric air intrusion. This signal is characterized by a subsidence pattern  
512 initiating late on 18 February, descending from near 100 hPa to approximately 250 hPa  
513 between 12Z on 18 February to 18Z on 19 February. This feature is further illustrated  
514 in Supplementary Figure S1b and c, where downward motion intersects the dynamic  
515 tropopause (defined by the -2 PVU surface) at 00Z and 06Z on 19 February, directly  
516 above the cyclone center. This subsidence contributes to the intensification of the mid-  
517 to-upper-level low, enhancing mass divergence aloft, as indicated by the FD profile  
518 (Supplementary Figure S2).

519 As the system transitions into a mature tropical cyclone, its dynamics depart from  
520 the QG framework and increasingly reflect a non-linear regime (González-Alemán  
521 et al., 2015). This transition is initiated by the deepening of the cutoff low and its  
522 vertical alignment with the surface cyclone, combined with stratospheric intrusions.  
523 The cutoff low contributes to the reduction of vertical wind shear and facilitates

524 the organization of deep convection, while the associated PV anomaly enhances the  
 525 development of a vertically coherent cyclonic structure (Hulme and Martin, 2009a;  
 526 González-Alemán et al., 2015). This, in turn, intensifies surface convergence and  
 527 promotes additional convective activity, increasing latent heat release and further  
 528 warming the tropospheric column. These processes establish a positive feedback loop  
 529 that accelerates the tropical transition (Emanuel, 1986). The tropical characteristics  
 530 of the cyclone are evident in Figures S1b and S1c, which display a classic vertical  
 531 structure marked by subsidence in the eye and deep convection concentrated along  
 532 the eyewall.

533 Furthermore, as the jet-like feature moves away from the region, the peak  $C_K$   
 534 conversions shift from the upper troposphere to the surface (Figure 10b). This is pos-  
 535 sibly associated with increased horizontal wind shear resulting from the convergence  
 536 of the southwesterly flow from the post-frontal high and the northeasterly flow from  
 537 the SASH near the cyclone center (Figure 12a).

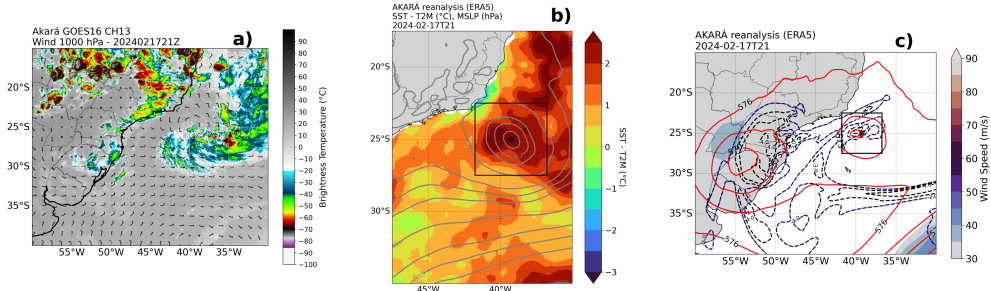


**Fig. 12** Synoptic conditions at 21Z on 17 February 2024, during the mid-intensification stage of the system. (a) Brightness temperature from GOES-16 Channel 13 (shading, in  $^{\circ}\text{C}$ ) and wind vectors at 1000 hPa. (b) Difference between sea surface temperature and 2-meter air temperature ( $\text{SST} - \text{T2M}$ ; shading, in  $^{\circ}\text{C}$ ) and mean sea level pressure (contours, in hPa). (c) Geopotential height at 500 hPa (red contours, in dam), wind speed at 200 hPa (shading, in  $\text{m s}^{-1}$ ), and potential vorticity at 200 hPa (dashed contours, in PVU). Black contours represent the -3 and -4 PVU levels, while the blue contour corresponds to the -2 PVU level. The black cross denotes the cyclone center. The black rectangles indicate the analysis domain used for the Lorenz Energy Cycle (LEC), heat budget, and vorticity budget diagnostics.

### 538 3.3 Mature Stage

539 During the mature phase, the CPS continues to indicate a deep warm-core structure  
 540 (Figure 4b). This structure becomes even more pronounced compared to the intensi-  
 541 fication phase, as shown in Figure 3. The surface layer becomes relatively warm, with  
 542 a particularly notable warming between 600 and 500 hPa. Meanwhile, the cyclone's  
 543 southward displacement brings it close to relatively cold waters (Figures 2 and 13b),  
 544 which stabilize the boundary layer, suppressing convection.

545 Despite a significant increase in anticyclonic vorticity advection near the surface  
 546 compared to the previous phase, cyclonic advection is now confined to two layers:

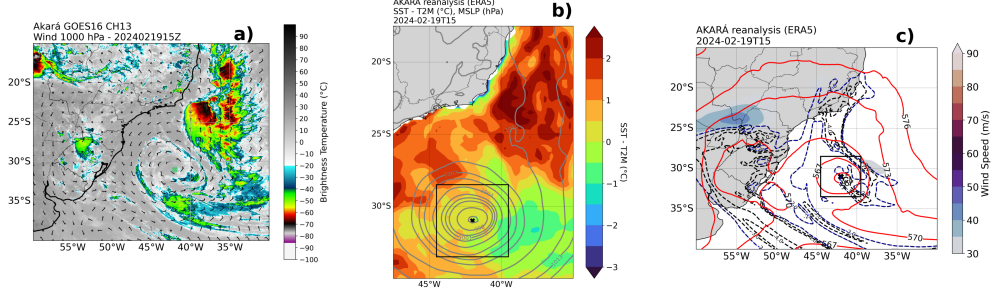


**Fig. 13** Synoptic conditions at 15Z on 19 February 2024, during the early-mature stage of the system. (a) Brightness temperature from GOES-16 Channel 13 (shading, in  $^{\circ}\text{C}$ ) and wind vectors at 1000 hPa. (b) Difference between sea surface temperature and 2-meter air temperature ( $\text{SST} - \text{T2M}$ ; shading, in  $^{\circ}\text{C}$ ) and mean sea level pressure (contours, in hPa). (c) Geopotential height at 500 hPa (red contours, in dam), wind speed at 200 hPa (shading, in  $\text{m s}^{-1}$ ), and potential vorticity at 200 hPa (dashed contours, in PVU). Black contours represent the  $-3$  and  $-4$  PVU levels, while the blue contour corresponds to the  $-2$  PVU level. The black cross denotes the cyclone center. The black rectangles indicate the analysis domain used for the Lorenz Energy Cycle (LEC), heat budget, and vorticity budget diagnostics.

547 between 700 and 500 hPa and between 200 and 150 hPa (Figure 7c). From a quasi-  
 548 geostrophic perspective, this configuration indicates an environment less favorable  
 549 for vertical motion than during the intensification phase. Consequently, the positive  
 550 values of the diabatic term become confined below the 300 hPa layer and decrease in  
 551 mean magnitude (Figure 9c). Similarly, the  $G_E$  term experiences a sharp decrease in  
 552 magnitude. This reduction in convective activity is also visible in satellite imagery,  
 553 which, despite displaying symmetric cloudiness around the cyclone center, shows lower  
 554 cloud tops compared to previous phases (Figure 13a).

555 The decrease in convective activity results in a cooling tendency above 400 hPa,  
 556 despite a warming tendency below this level (Figure 9c). The warming below 400 hPa  
 557 is supported by an increase in horizontal temperature advection, particularly above  
 558 800 hPa, where the total vertical motion effect nearly offsets the diabatic term. Above  
 559 200 hPa, a sharp increase in warm advection leads to a net warming tendency in the  
 560 upper troposphere.

561 Although the time-averaged total vertical motion effect term indicates a net cool-  
 562 ing contribution, the influence of stratospheric intrusion becomes evident through the  
 563 total vertical motion effect term (Figure 10a). Concurrently, potential vorticity val-  
 564 ues as low as  $-4$  PVU are observed near the cyclone center (Figure 13c), indicating  
 565 a significantly lowered tropopause. This interaction promotes a warming effect that  
 566 propagates downward from the upper atmospheric layers to approximately 200 hPa.  
 567 The surface fluxes, although present, were insufficient to sustain deep convective activ-  
 568 ity capable of warming the upper troposphere. Instead, the stratosphere-troposphere  
 569 interactions played a significant role in contributing to the observed warming of the  
 570 mid-upper troposphere.

571 At this stage, a moderate anticyclonic tendency is observed throughout the tropo-  
 572 sphere, consistent with the system no longer intensifying. Near the surface, FD and

especially ZD strongly contribute to cyclonic tendencies, indicating mass convergence, but these are counterbalanced by intense anticyclonic horizontal advection and the residual term. Throughout most of the atmospheric column up to 200 hPa, the residual term and vertical vorticity advection contribute cyclonically but are offset by the tilting term, which shows a sharp increase in magnitude compared to previous phases. As discussed by Dutra et al. (2017), the tilting term is often negligible in synoptic-scale motions, but its prominence in Akará's mature phase indicates the system's mesoscale characteristics as a tropical cyclone. Its high values also suggest increased vertical wind shear, driven by intense surface winds (Reboita et al., 2024). Above 200 hPa, FD becomes the primary contributor to the anticyclonic tendency, indicating mass divergence, albeit confined to a narrower layer compared to earlier phases.

From an energetic perspective, Akará's environment becomes fully barotropic, characterized by negative  $C_Z$  and  $C_A$  conversions. These terms reflect a reduction in environmental north-south temperature gradients, despite ongoing meridional heat transport and residual convective activity (Figure 13a). Barotropic conversions, similar to the intensification phase, remain the primary energy source for Akará, with a twofold increase in magnitude. This is accompanied by a comparable increase in the  $RK_Z$  term and a fourfold increase in  $RK_E$ . The increase in  $RK_E$  is associated with higher dissipation rates, as indicated by the  $F_\zeta$  term, which transfers momentum to the sea surface and generates high sea waves (Zhao et al., 2022; Shimura et al., 2024, e.g.). For  $RK_Z$ , the large values may be linked to energy upscale transfer from subgrid to grid-scale processes, as suggested by Michaelides (1987). However, since this term also includes numerical errors and other unresolved processes, this interpretation remains speculative.

The dissipation of  $K_E$ , combined with energy exports, results in an overall negative budget for this term as the system reaches its maximum intensity and transitions into the decay stage. Notably, barotropic conversions during the mature phase occur throughout almost the entire troposphere, with strong values extending from near the surface up to 500 hPa (Figure 10b). These conversions may have been enhanced by the strong horizontal wind shear near the cyclone center as it reached peak intensity, as well as by vertical wind shear, as evidenced by the tilting term.

### 3.4 Decay stage

Akará enters the decay phase still classified as a tropical cyclone, as evidenced by the CPS (Figure 4). However, the zonal mean temperature deviation profile shows the emergence of an upper-level cold anomaly (Figure 3). From approximately 15Z on February 21 onward, this upper-level cold anomaly intensifies and extends into the mid-troposphere, marking the system's subtropical transition. Accordingly, the CPS indicates a shift from a deep to a shallow warm core during this process, as the system moves over relatively cold waters (Figures 2 and 14b).

At this stage, both the vorticity and heat budgets show sharp decreases in the magnitude of all terms. The relatively modest values of FD, ZD,  $F_\zeta$ , and horizontal vorticity advection reflect their previously high magnitudes near the mature phase, which gradually diminish over time. Meanwhile, the system's energy cycle highlights a significant environmental shift, with the conversion terms  $C_Z$ ,  $C_A$ , and  $C_E$  changing

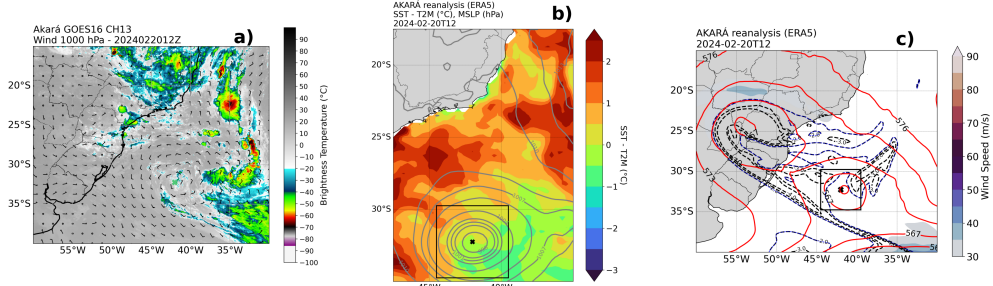


**Fig. 14** Synoptic conditions at 12Z on 22 February 2024, during the early-mature stage of the system. (a) Brightness temperature from GOES-16 Channel 13 (shading, in  $^{\circ}\text{C}$ ) and wind vectors at 1000 hPa. (b) Difference between sea surface temperature and 2-meter air temperature ( $\text{SST} - \text{T2M}$ , shading, in  $^{\circ}\text{C}$ ) and mean sea level pressure (contours, in hPa). (c) Geopotential height at 500 hPa (red contours, in dam), wind speed at 200 hPa (shading, in  $\text{m s}^{-1}$ ), and potential vorticity at 200 hPa (dashed contours, in PVU). Black contours represent the  $-3$  and  $-4$  PVU levels, while the blue contour corresponds to the  $-2$  PVU level. The black cross denotes the cyclone center. The black rectangles indicate the analysis domain used for the Lorenz Energy Cycle (LEC), heat budget, and vorticity budget diagnostics.

sign (Figure 8d). Additionally, there are sharp increases in  $K_Z$  imports, while the  $A_Z$  flux across the boundaries also becomes positive. These changes indicate that the decaying system is approaching a weak baroclinic region associated with an upper-level trough at higher latitudes (Figure 14c). Initially, barotropic conversions remain high, particularly up to 600 hPa, but as the system moves closer to the trough, these conversions shift to upper levels (Figure 10b).

These atmospheric changes, combined with the system's displacement over relatively cold waters, result in a decrease in convective activity. Consequently, convection near the cyclone center loses its organized structure, and cloud tops become relatively warmer (Figure 14a). Notably, a stratospheric incursion occurs at the onset of the decay phase (Figure 10a). However, without sufficient low-level forcing, this incursion is insufficient to sustain convective activity.

## 4 Discussion and Concluding Remarks

Cyclone Akará originated in a post-frontal, weak baroclinic environment with low vertical wind shear and warm SSTs. During its genesis, SSTs exceeded the  $26.5^{\circ}\text{C}$  threshold, traditionally considered necessary for tropical cyclone development (Gray, 1968; Emanuel, 1986). Although the initial convective activity was linked to the remaining frontal system, the thermal contrast between the cold post-frontal lower troposphere and warm SSTs fueled sensible and latent heat fluxes, which, in turn, sustained Akará's convective activity. Furthermore, a mid-upper tropospheric cutoff low coupled with the surface vortex during this stage, resulting in a subtropical genesis characterized by a weak symmetric warm core, as indicated by Reboita et al. (2024).

Notably, Akará's genesis as a subtropical cyclone was somewhat distinct compared to other subtropical systems. For instance, it was not associated with a mid-to-upper

troposphere blocking pattern, a common feature of subtropical cyclogenesis across various ocean basins (da Rocha et al., 2019). Additionally, the development of Tropical Depression Iba and Hurricane Catarina, the only other documented tropical cyclones in the South Atlantic, was linked to such synoptic conditions (Pezza and Simmonds, 2005; Reboita et al., 2021). However, other key ingredients identified by da Rocha et al. (2019), such as isolation from baroclinic influences, persistent ocean-to-atmosphere heat fluxes, and low environmental vertical wind shear, were present during Akará's initial stages. Moreover, the initial energetics of the system — characterized by contributions to eddy kinetic energy from both barotropic and baroclinic chains — align with findings for other subtropical and hybrid systems (Michaelides, 1987; Dias Pinto et al., 2013; Pezza et al., 2014; Cavicchia et al., 2018).

The system's intensification phase was marked by increased near-surface mass convergence and upper-level mass divergence, which favored upward motion and enhanced convective activity. This occurred as the system moved into a region with SSTs above 28°C. The further reduction in vertical wind shear supported the organization of convection into a spiral pattern, with Akará developing a barotropic structure. The environment also transitioned to being less baroclinic and more barotropic, with mid to low-level barotropic conversions playing a key role in fueling the system's development.

During the intensification phase, Akará underwent tropical transition, evolving to exhibit a deep warm core. This transition coincided with an increased thermal contrast between the ocean and atmosphere, which further enhanced near-surface heat fluxes, reducing stability and promoting convective activity. While convective processes undoubtedly contributed to heating the atmospheric column, we propose that stratospheric air intrusions were critical to the tropospheric heating that characterized Akará's tropical transition. High-PV air descended across the tropopause, which promotes intensification the surface cyclone (Hoskins et al., 1985; Hulme and Martin, 2009a; Davis and Bosart, 2003). Also, the mid-to-upper cyclonic circulation helped in reducing the vertical wind-shear, promoting the organization of the precipitation, which resulted the cyclone in acquiring a tropical structure, with air descending in the center of the eye and ascending on the eye walls (Figures S1b and c). The stratospheric intrusions of high-PV air across the tropopause induce surface pressure falls and low-level cyclonic circulation via balanced PV inversion (Hoskins et al., 1985; Davis, 1992), while subsequent diabatic processes redistribute PV vertically, especially creating low-level PV, thereby enhancing vertical coherence and cyclone intensification. (Stoelinga, 1996; Hulme and Martin, 2009a,b; Davis and Bosart, 2003). Additionally, the mid-to-upper-level cyclonic circulation contributed to a reduction in vertical wind shear, facilitating the organization of precipitation and promoting the development of a tropical structure, with subsidence at the center of the eye and deep convection along the eyewall (Figures S1b and S1c).

The dynamical origins of these intrusions warrant further investigation, and we recommend future studies employing numerical simulations to assess their relative importance for Akará's tropical transition. Moreover, the role of stratosphere-troposphere interactions during Catarina's tropical transition has not yet been explored. Determining whether such interactions are fundamental to tropical transitions in the South

686     Atlantic is crucial for improving our understanding and forecasting of these rare  
687     events.

688     The cyclone reached its mature phase with warm anomalies throughout the tro-  
689     posphere, intensifying its deep warm-core structure. The system's cloudiness became  
690     fully detached from the preceding frontal structure and exhibited an eye, as reported  
691     by the Brazilian Navy (Marinha do Brasil, 2024). However, during this phase, con-  
692     vective activity decreased compared to earlier stages as the system moved over colder  
693     waters (below 25°C), despite increased near-surface mass convergence. Stratospheric  
694     air intrusions persisted during the mature phase and may have contributed to main-  
695     taining the observed warm-core structure, compensating for the reduced latent heat  
696     release. The signature of these intrusions is visible in the total vertical motion effect  
697     but is less evident in the heat budget due to period averaging.

698     Although barotropic conversions increased significantly during the mature phase,  
699     high surface friction and the export of eddy kinetic energy acted as brakes on further  
700     development. Notably, barotropic conversions were intense from the surface to the  
701     mid-troposphere, while the baroclinic chain remained inactive, reflecting the cyclone's  
702     barotropic environment. This transition of barotropic conversions, shifting from the  
703     upper troposphere to the mid-to-low levels, was also observed during Catarina's trop-  
704     ical transition (Veiga et al., 2008). While studies analyzing the evolution of barotropic  
705     instability profiles in tropical cyclones remain scarce, numerical and observational  
706     evidence indicates that low-level barotropic instability is a primary mechanism asso-  
707     ciated with initial vortex formation in tropical disturbances within the Intertropical  
708     Convergence Zone (ITCZ), which often serve as precursors to tropical cyclones (Fer-  
709     reira and Schubert, 1997; Yokota et al., 2012, 2015; Bembeneck et al., 2021). Beyond  
710     the ITCZ, African Easterly Waves, which are precursors to tropical cyclones in the  
711     Northern Atlantic, are also strongly linked to mid-to-low-level barotropic instability  
712     (Burpee, 1972; Rennick, 1976; Molinari et al., 1997; Reed et al., 1977; Wu et al.,  
713     2012). These connections highlight the critical role of barotropic processes in trop-  
714     ical cyclone genesis. Further research is necessary to investigate the role of barotropic  
715     instability and its vertical distribution in tropical cyclones, particularly in regions like  
716     the South Atlantic where these systems are rare. A more comprehensive under-  
717     standing of these dynamics could improve our knowledge of the mechanisms driving vortex  
718     formation and development, ultimately enhancing predictions of tropical cyclogenesis  
719     and evolution in underexplored basins.

720     Following its mature phase, Akará experienced further reductions in convective  
721     activity, as the system's cloudiness lost its organizational structure. This decay phase  
722     was marked by sharp decreases in both heat and vorticity budget terms, as well as  
723     environmental changes near the cyclone center, with the system approaching a baro-  
724     clinic zone. Barotropic conversions diminished during this phase, shifting from peaking  
725     near the surface to occurring at upper levels. During its decay, Akará underwent sub-  
726     tropical transition, marked by cooling in the mid-to-upper troposphere, movement  
727     over colder waters (below 23°C), and displacement into a colder atmospheric region  
728     at lower latitudes (below 32°S).

Nevertheless, it is important to acknowledge limitations of the present study. The semi-Lagrangian, storm-following domain does not explicitly account for spatial variations in the background APE and KE along the track, which may influence  $A_Z$ ,  $K_Z$  and their lateral-flux and pressure-work boundary terms. In addition, the LEC employs a global reference state for APE, which may constrain some interpretations of local energetics (e.g., Smith, 1980). Although recently proposed local formulations, based on parcelwise reference states, can reveal locally generated APE and thus complement our diagnosis (Novak and Tailleux, 2018; Federer et al., 2024), global energy fluxes appear broadly consistent between global and local approaches (e.g., Liu et al., 2024). Finally, although the limited-area LEC does not explicitly resolve downstream development, it might be expressed through LEC energy imports, as suggested by Michaelides et al. (1999). A complementary analysis following the framework of Orlanski and Katzfey (1991) with a time-mean basic state would better isolate downstream propagation and could be pursued in future work.

In conclusion, this study provides valuable insights into the dynamical, thermodynamical and energetic features of a rare tropical transition event in the South Atlantic, as suggested by Reboita et al. (2024). The analysis of Akará's life cycle phases proved valuable for understanding the dynamic, thermodynamic, and environmental shifts during its development, complementing the thermal structure analysis that highlighted the cyclone's transition from a subtropical to a tropical system. Future research focusing on similar tropical transition events could enhance our understanding of the mechanisms underlying these processes, particularly in the South Atlantic, where such occurrences are rare. Comparative studies with other tropical transitions, such as those of Hurricane Catarina and Tropical Depression Iba, or with subtropical cyclones that did not undergo tropical transition, could offer valuable perspectives on the conditions and factors influencing these systems. Such research would also contribute to improved forecasting and risk assessment for similar events in the future.

## Declarations

### Funding

This study was partly financed by the Coordenação de Aperfeiçoamento de Pessoal de Nível Superior – Brasil (CAPES) under Finance Code 001.

### Competing interests

The authors have no relevant financial or non-financial interests to disclose.

### Data Availability

The data supporting the findings of this study, including the results of the Lorenz Energy Cycle and the heat and vorticity budget analyses, are openly available in the following repositories. The complete diagnostics and plotting scripts for Cyclone Akará are available at: [https://github.com/Victorran/Cyclone\\_Analysis/tree/main/Akara](https://github.com/Victorran/Cyclone_Analysis/tree/main/Akara). The LorenzCycleToolkit, used to compute the Lorenz Energy Cycle, is available at: <https://github.com/daniloceano/LorenzCycleToolkit>. The ATMOS-BUD framework,

769 used for calculating heat and vorticity budgets, is available at: <https://github.com/danioloceano/ATMOS-BUD>. All datasets and scripts are publicly accessible and can  
 770 be used to reproduce the analyses presented in this manuscript.  
 771

## 772 Author contributions

- 773 • **Danilo Couto de Souza:** Conceptualization, Methodology, Software, Formal  
 774 Analysis, Investigation, Writing - Original Draft, Writing - Review & Editing.  
 775 • **Victor Antunes Ranieri:** Formal Analysis, Data Curation, Investigation.  
 776 • **Pedro Leite da Silva Dias:** Supervision, Writing - Review & Editing, Method-  
 777 ology, Analysis Support.  
 778 • **Andrés Rodríguez Flores:** Formal Analysis, Data Curation, Investigation.  
 779 • **Ricardo de Camargo:** Supervision, Writing - Review & Editing, Analysis  
 780 Support.

## 781 Supplementary information

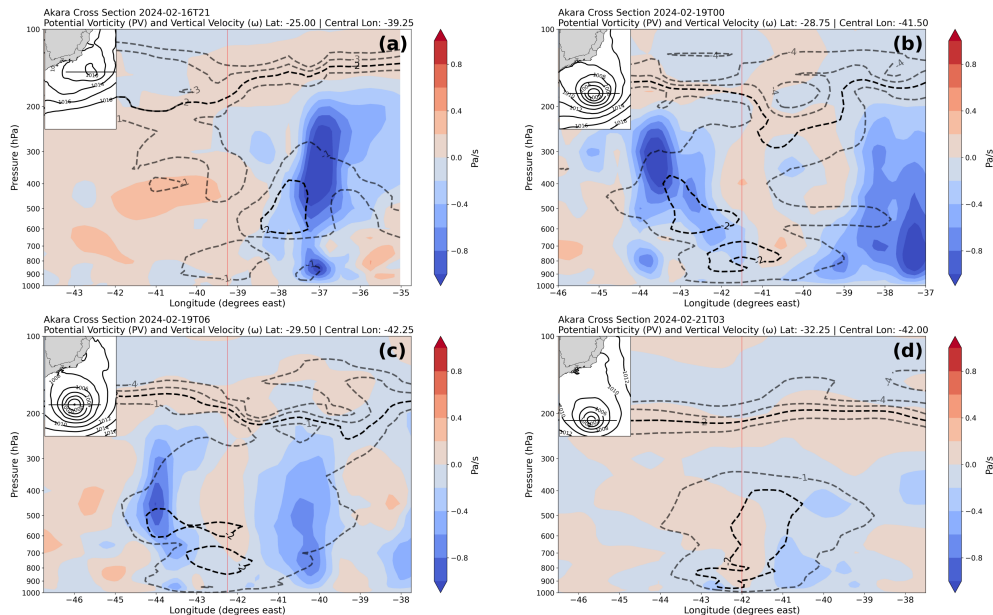


**Fig. S1** Vertical cross-sections of potential vorticity (PV, dashed contours, in PVU) and vertical velocity ( $\omega$ , shading, in  $\text{Pa s}^{-1}$ ) at selected times during the development of Akará. Gray contours denote the -3 and -4 PVU levels, while the black contour represents the -2 PVU surface, typically used to approximate the dynamic tropopause. Embedded maps show the corresponding surface pressure fields and cross-section locations.

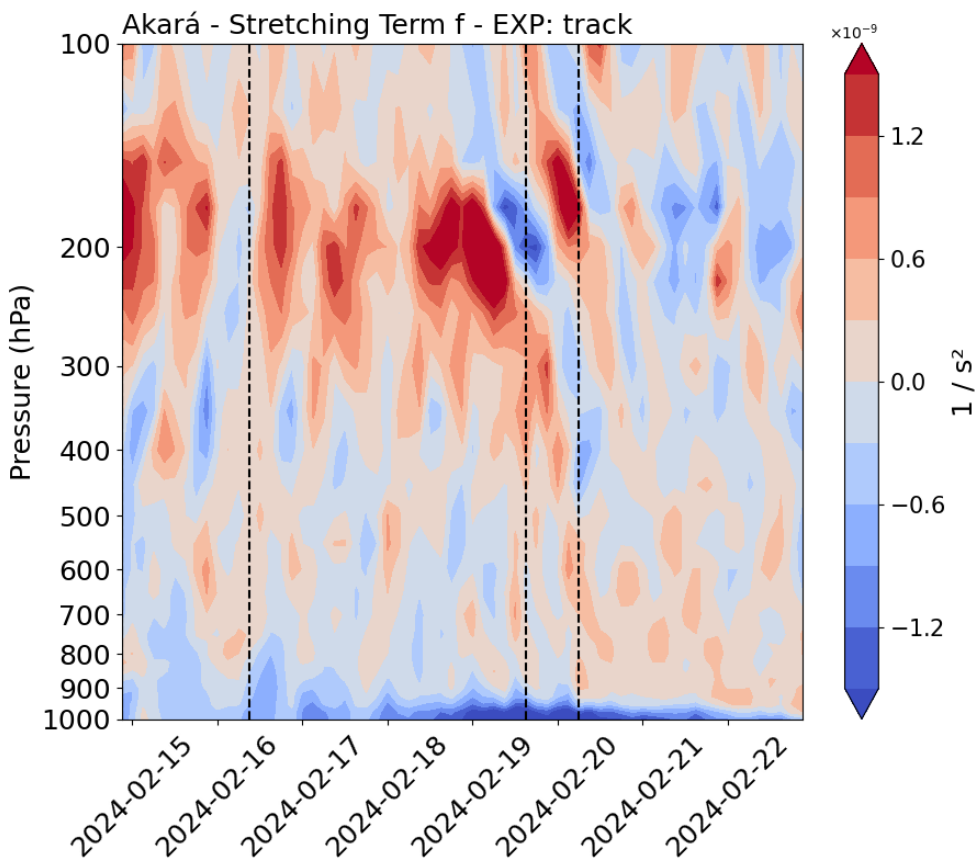


**Fig. S2** Time–pressure Hovmöller diagram of the planetary vorticity contribution to the stretching term (FD) along the Akará track, from February 14 to 22, 2024. Shading represents values in  $s^{-2}$ , Dashed vertical lines mark phase transitions in the cyclone life cycle.

## 782 References

- 783 Andrelina Silva, B. and M. Simões Reboita. 2021. Climatologia do índice do potencial  
 784 de gênese de ciclones tropicais nos oceanos adjacentes à américa do sul. *Anuário  
 785 do Instituto de Geociências* 44 .
- 786 Baray, J.L., G. Ancellet, T. Randriambelo, and S. Baldy. 1999. Tropical cyclone  
 787 marlene and stratosphere-troposphere exchange. *Journal of Geophysical Research: Atmospheres* 104(D11): 13953–13970 .
- 788 Barnes, M.A., T. Ndarana, M. Sprenger, and W.A. Landman. 2022. Stratospheric  
 789 intrusion depth and its effect on surface cyclogenetic forcing: an idealized potential  
 790 vorticity (pv) inversion experiment. *Weather and Climate Dynamics* 3(4): 1291–  
 791 1309 .
- 792

- 793 Bembeneck, E., T.M. Merlis, and D.N. Straub. 2021. Influence of latitude and moisture  
794 effects on the barotropic instability of an idealized itcz. *Journal of the Atmospheric*  
795 *Sciences* 78(9): 2677–2689 .
- 796 Black, M.T. and A.B. Pezza. 2013. A universal, broad-environment energy conversion  
797 signature of explosive cyclones. *Geophysical Research Letters* 40(2): 452–457 .
- 798 Brennan, F.E. and D.G. Vincent. 1980. Zonal and eddy components of the synoptic-  
799 scale energy budget during intensification of hurricane carmen (1974). *Monthly*  
800 *Weather Review* 108(7): 954–965. [https://doi.org/10.1175/1520-0493\(1980\)  
801 108<0954:ZAECOT>2.0.CO;2](https://doi.org/10.1175/1520-0493(1980)108<0954:ZAECOT>2.0.CO;2) .
- 802 Bulic, I. 2006. Limited area energy budget during a life cycle of genoa cyclone  
803 (18-21 november 1999). *NUOVO CIMENTO-SOCIETA ITALIANA DI FISICA*  
804 *SEZIONE C* 29(2): 167 .
- 805 Burpee, R.W. 1972. The origin and structure of easterly waves in the lower troposphere  
806 of north africa. *Journal of the Atmospheric Sciences* 29(1): 77–90 .
- 807 Camargo, S., A.H. Sobel, A.G. Barnston, and K.A. Emanuel. 2007. Tropical cyclone  
808 genesis potential index in climate models. *Tellus A: Dynamic Meteorology and*  
809 *Oceanography* 59(4): 428–443 .
- 810 Cardoso, A.A., R.P. da Rocha, and N.M. Crespo. 2022. Synoptic climatology of  
811 subtropical cyclone impacts on near-surface winds over the south atlantic basin.  
812 *Earth and Space Science* 9(11): e2022EA002482 .
- 813 Cavicchia, L., A. Dowdy, and K. Walsh. 2018. Energetics and dynamics of sub-  
814 tropical australian east coast cyclones: Two contrasting cases. *Monthly Weather*  
815 *Review* 146(5): 1511–1525 .
- 816 Chu, J.H., M. Yanai, and C.H. Sui. 1981. Effects of cumulus convection on the vorticity  
817 field in the tropics part i: The large-scale budget. *Journal of the Meteorological*  
818 *Society of Japan. Ser. II* 59(4): 535–546 .
- 819 da Rocha, R.P., M.S. Reboita, L.F. Gozzo, L.M.M. Dutra, and E.M. de Jesus. 2019.  
820 Subtropical cyclones over the oceanic basins: a review. *Annals of the New York*  
821 *Academy of Sciences* 1436(1): 138–156 .
- 822 Davis, C.A. 1992. Piecewise potential vorticity inversion. *Journal of Atmospheric*  
823 *Sciences* 49(16): 1397–1411 .
- 824 Davis, C.A. and L.F. Bosart. 2003. Baroclinically induced tropical cyclogenesis.  
825 *Monthly Weather Review* 131(11): 2730–2747 .
- 826 de Jesus, E.M., R.P. da Rocha, N.M. Crespo, M.S. Reboita, and L.F. Gozzo. 2022.  
827 Future climate trends of subtropical cyclones in the south atlantic basin in an

- 828 ensemble of global and regional projections. *Climate Dynamics* 58(3): 1221–1236 .
- 829 de Souza, D.C., P.L.S. da Dias, M.B.L. da Silva, and R. de Camargo. 2024. Lorenz-  
830 cycle toolkit: A comprehensive python tool for analyzing atmospheric energy cycles.  
831 *Journal of Open Source Software* 9(101): 7139 .
- 832 de Souza, D.C., P.L.S. da Dias, C.B. Gramcianinov, and R. de Camargo. 2025.  
833 Cyclophaser: A python package for detecting extratropical cyclone life cycles.  
834 *Journal of Open Source Software* 10(108): 7363 .
- 835 de Souza, D.C., P.L. da Silva Dias, C.B. Gramcianinov, and R. Camargo. 2025. Lorenz  
836 energy cycle climatology for the southwestern atlantic cyclones. *EarthArXiv* .
- 837 de Souza, D.C., P.L. da Silva Dias, C.B. Gramcianinov, M.B.L. da Silva, and  
838 R. de Camargo. 2024. New perspectives on south atlantic storm track through  
839 an automatic method for detecting extratropical cyclones' lifecycle. *International  
840 Journal of Climatology* 44(10): 3568–3588 .
- 841 de Souza, D.C., P.L. da Silva Dias, and R. Hallak. 2025. Atmos-bud: A comprehensive  
842 python tool for analyzing heat, vorticity, and water budgets on the atmosphere.  
843 *Journal of Open Source Software* .
- 844 DesRosiers, A.J., M.M. Bell, and T.Y. Cha. 2022. Vertical vortex development in hur-  
845 rricane michael (2018) during rapid intensification. *Monthly Weather Review* 150(1):  
846 99–114 .
- 847 Dias Pinto, J.R., M.S. Reboita, and R.P. da Rocha. 2013. Synoptic and dynam-  
848 ical analysis of subtropical cyclone anita (2010) and its potential for tropical  
849 transition over the south atlantic ocean. *Journal of Geophysical Research:  
850 Atmospheres* 118(19): 10–870. <https://doi.org/10.1002/jgrd.50830> .
- 851 Dias Pinto, J.R. and R.P. Rocha. 2011. The energy cycle and structural evolu-  
852 tion of cyclones over southeastern south america in three case studies. *Journal of  
853 Geophysical Research: Atmospheres* 116(D14) .
- 854 Dutra, L.M.M., R.P. da Rocha, R.W. Lee, J.R.R. Peres, and R. de Camargo. 2017.  
855 Structure and evolution of subtropical cyclone anita as evaluated by heat and vor-  
856 ticity budgets. *Quarterly Journal of the Royal Meteorological Society* 143(704):  
857 1539–1553 .
- 858 Emanuel, K.A. 1986. An air-sea interaction theory for tropical cyclones. part i: Steady-  
859 state maintenance. *Journal of Atmospheric Sciences* 43(6): 585–605 .
- 860 Fang, J., O. Pauluis, and F. Zhang. 2019. The thermodynamic cycles and associated  
861 energetics of hurricane edouard (2014) during its intensification. *Journal of the  
862 Atmospheric Sciences* 76(6): 1769–1784 .

- 863 Federer, M., L. Papritz, M. Sprenger, C.M. Grams, and M. Wenta. 2024. On the local  
864 available potential energy perspective of baroclinic wave development. *Journal of*  
865 *the Atmospheric Sciences* 81(5): 871–886 .
- 866 Ferrara, M., F. Groff, Z. Moon, K. Keshavamurthy, S.M. Robeson, and C. Kieu.  
867 2017. Large-scale control of the lower stratosphere on variability of tropical cyclone  
868 intensity. *Geophysical Research Letters* 44(9): 4313–4323 .
- 869 Ferreira, R.N. and W.H. Schubert. 1997. Barotropic aspects of itcz breakdown.  
870 *Journal of the Atmospheric Sciences* 54(2): 261–285 .
- 871 Gan, M.A. and V.B. Rao. 1991. Surface cyclogenesis over south america. *Monthly*  
872 *Weather Review* 119(5): 1293–1302 .
- 873 González-Alemán, J.J., F. Valero, F. Martín-León, and J.L. Evans. 2015. Classification  
874 and synoptic analysis of subtropical cyclones within the northeastern atlantic ocean.  
875 *Journal of Climate* 28(8): 3331–3352 .
- 876 Gozzo, L., R. Da Rocha, L. Gimeno, and A. Drumond. 2017. Climatology and  
877 numerical case study of moisture sources associated with subtropical cyclogenesis  
878 over the southwestern atlantic ocean. *Journal of Geophysical Research: Atmospheres*  
879 122(11): 5636–5653 .
- 880 Gozzo, L.F., R.P. da Rocha, M.S. Reboita, and S. Sugahara. 2014. Subtropical  
881 cyclones over the southwestern south atlantic: Climatological aspects and case  
882 study. *Journal of Climate* 27(22): 8543–8562 .
- 883 Gramcianinov, C., K. Hodges, and R.d. Camargo. 2019. The properties and genesis  
884 environments of south atlantic cyclones. *Climate Dynamics* 53: 4115–4140 .
- 885 Gray, W.M. 1968. Global view of the origin of tropical disturbances and storms.  
886 *Monthly Weather Review* 96(10): 669–700 .
- 887 Hamouda, M.E. and F. Kucharski. 2019. Ekman pumping mechanism driving precipi-  
888 tation anomalies in response to equatorial heating. *Climate Dynamics* 52: 697–711  
889 .
- 890 Hart, R.E. 2003. A cyclone phase space derived from thermal wind and thermal  
891 asymmetry. *Monthly weather review* 131(4): 585–616 .
- 892 Hersbach, H., B. Bell, P. Berrisford, S. Hirahara, A. Horányi, J. Muñoz-Sabater,  
893 J. Nicolas, C. Peubey, R. Radu, D. Schepers, et al. 2020. The era5 global reanalysis.  
894 *Quarterly Journal of the Royal Meteorological Society* 146(730): 1999–2049 .
- 895 Hoskins, B.J. and K.I. Hodges. 2002. New perspectives on the northern hemisphere  
896 winter storm tracks. *Journal of the Atmospheric Sciences* 59(6): 1041–1061. [https://doi.org/10.1175/1520-0469\(2002\)059<1041:NPOTNH>2.0.CO;2](https://doi.org/10.1175/1520-0469(2002)059<1041:NPOTNH>2.0.CO;2) .

- 898 Hoskins, B.J., M.E. McIntyre, and A.W. Robertson. 1985. On the use and significance  
 899 of isentropic potential vorticity maps. *Quarterly Journal of the Royal Meteorological*  
 900 *Society* 111(470): 877–946 .
- 901 Hulme, A.L. and J.E. Martin. 2009a. Synoptic-and frontal-scale influences on tropical  
 902 transition events in the atlantic basin. part i: A six-case survey. *Monthly weather*  
 903 *review* 137(11): 3605–3625 .
- 904 Hulme, A.L. and J.E. Martin. 2009b. Synoptic-and frontal-scale influences on tropical  
 905 transition events in the atlantic basin. part ii: Tropical transition of hurricane karen.  
 906 *Monthly weather review* 137(11): 3626–3650 .
- 907 Liu, Z., C.L. Franzke, L. Novak, R. Tailleux, and V. Lembo. 2024. A systematic  
 908 local view of the long-term changes in the atmospheric energy cycle. *Journal of*  
 909 *Climate* 37(23): 6413–6434 .
- 910 Lorenz, E. 1967. The nature and theory of the general circulation of the atmosphere.  
 911 *World meteorological organization* 161 .
- 912 Maddox, R.A. and C.A. Doswell III. 1982. An examination of jet stream configura-  
 913 tions, 500 mb vorticity advection and low-level thermal advection patterns during  
 914 extended periods of intense convection. *Monthly Weather Review* 110(3): 184–197 .
- 915 Marinha do Brasil, C.d.H.d.M. 2024, feb. Tempes-  
 916 tade tropical akará: Relatório pós-evento. Available at:  
 917 [https://www.marinha.mil.br/chm/sites/www.marinha.mil.br.chm/files/u1894/relatorio\\_pos\\_evento\\_akara.pdf](https://www.marinha.mil.br/chm/sites/www.marinha.mil.br.chm/files/u1894/relatorio_pos_evento_akara.pdf).
- 918 Marrafon, V.H., M.S. Reboita, R.P. da Rocha, and E.M. de Jesus. 2022. Classificação  
 919 dos tipos de ciclones sobre o oceano atlântico sul em projeções com o regcm4 e  
 920 mcgs. *Revista Brasileira de Climatologia* 30: 1–25 .
- 921 May, R.M., K.H. Goebbert, J.E. Thielen, J.R. Leeman, M.D. Camron, Z. Bruick, E.C.  
 922 Bruning, R.P. Manser, S.C. Arms, and P.T. Marsh. 2022. Metpy: A meteorolog-  
 923 ical python library for data analysis and visualization. *Bulletin of the American*  
 924 *Meteorological Society* 103(10): E2273–E2284 .
- 925 McTaggart-Cowan, R., L.F. Bosart, C.A. Davis, E.H. Atallah, J.R. Gyakum, and  
 926 K.A. Emanuel. 2006. Analysis of hurricane catarina (2004). *Monthly Weather*  
 927 *Review* 134(11): 3029–3053 .
- 928 Michaelides, S.C. 1987. Limited area energetics of genoa cyclogenesis. *Monthly*  
 929 *Weather Review* 115(1): 13–26 .
- 930 Michaelides, S.C. 1992. A spatial and temporal energetics analysis of a baroclinic  
 931 disturbance in the mediterranen. *Monthly weather review* 120(7): 1224–1243 .

- 932 Michaelides, S.C., N.G. Prezerakos, and H.A. Flocas. 1999. Quasi-lagrangian ener-  
 933 getics of an intense mediterranean cyclone. *Quarterly Journal of the Royal*  
 934 *Meteorological Society* 125(553): 139–168 .
- 935 Molinari, J., D. Knight, M. Dickinson, D. Vollaro, and S. Skubis. 1997. Potential  
 936 vorticity, easterly waves, and eastern pacific tropical cyclogenesis. *Monthly weather*  
 937 *review* 125(10): 2699–2708 .
- 938 Montgomery, M.T., Z. Wang, and T.J. Dunkerton. 2010. Coarse, intermediate and  
 939 high resolution numerical simulations of the transition of a tropical wave critical  
 940 layer to a tropical storm. *Atmospheric Chemistry and Physics* 10(22): 10803–10827  
 941 .
- 942 Moon, Z. and C. Kieu. 2017. Impacts of the lower stratosphere on the development  
 943 of intense tropical cyclones. *Atmosphere* 8(7): 128 .
- 944 Muench, H.S. 1965. On the dynamics of the wintertime stratosphere circulation.  
 945 *Journal of Atmospheric Sciences* 22(4): 349–360 .
- 946 Novak, L. and R. Tailleux. 2018. On the local view of atmospheric available potential  
 947 energy. *Journal of the Atmospheric Sciences* 75(6): 1891–1907 .
- 948 Ohno, T. and M. Satoh. 2015. On the warm core of a tropical cyclone formed near  
 949 the tropopause. *Journal of the Atmospheric Sciences* 72(2): 551–571 .
- 950 Orlanski, I. and J. Katzfey. 1991. The life cycle of a cyclone wave in the southern  
 951 hemisphere. part i: Eddy energy budget. *Journal of Atmospheric Sciences* 48(17):  
 952 1972–1998 .
- 953 Pereira Filho, A.J., A.B. Pezza, I. Simmonds, R.S. Lima, and M. Vianna. 2010.  
 954 New perspectives on the synoptic and mesoscale structure of hurricane catarina.  
 955 *Atmospheric Research* 95(2-3): 157–171 .
- 956 Pezza, A.B., L.A. Garde, J.A.P. Veiga, and I. Simmonds. 2014. Large scale features  
 957 and energetics of the hybrid subtropical low ‘duck’over the tasman sea. *Climate*  
 958 *dynamics* 42: 453–466 .
- 959 Pezza, A.B. and I. Simmonds. 2005. The first south atlantic hurricane: Unprecedented  
 960 blocking, low shear and climate change. *Geophysical Research Letters* 32(15) .
- 961 Pezza, A.B., I. Simmonds, and A.J. Pereira Filho. 2009. Climate perspective on the  
 962 large-scale circulation associated with the transition of the first south atlantic hur-  
 963 rricane. *International Journal of Climatology: A Journal of the Royal Meteorological*  
 964 *Society* 29(8): 1116–1130 .
- 965 Pezza, A.B., J.A.P. Veiga, I. Simmonds, K. Keay, and M.d.S. Mesquita. 2010. Envi-  
 966 ronmental energetics of an exceptional high-latitude storm. *Atmospheric Science*

- 967      *Letters* 11(1): 39–45 .
- 968      Pezzi, L.P., R.B. de Souza, O. Acevedo, I. Wainer, M.M. Mata, C.A. Garcia, and  
969      R. de Camargo. 2009. Multiyear measurements of the oceanic and atmospheric  
970      boundary layers at the brazil-malvinas confluence region. *Journal of Geophysical  
971      Research: Atmospheres* 114(D19) .
- 972      Pezzi, L.P., R.B. de Souza, M.F. Santini, A.J. Miller, J.T. Carvalho, C.K. Parise, M.F.  
973      Quadro, E.B. Rosa, F. Justino, U.A. Sutil, et al. 2021. Oceanic eddy-induced mod-  
974      ifications to air-sea heat and co2 fluxes in the brazil-malvinas confluence. *Scientific  
975      reports* 11(1): 10648 .
- 976      Raymond, D. and C. López Carrillo. 2011. The vorticity budget of developing typhoon  
977      nuri (2008). *Atmospheric Chemistry and Physics* 11(1): 147–163 .
- 978      Reboita, M., N. Crespo, L. Dutra, B. Silva, B. Capucin, and R. da Rocha. 2021. Iba:  
979      the first pure tropical cyclogenesis over the western south atlantic ocean. *Journal of  
980      Geophysical Research: Atmospheres* 126(1): e2020JD033431 .
- 981      Reboita, M.S., R.P. Da Rocha, T. Ambrizzi, and S. Sugahara. 2010. South atlantic  
982      ocean cyclogenesis climatology simulated by regional climate model (regcm3).  
983      *Climate Dynamics* 35: 1331–1347 .
- 984      Reboita, M.S., L.F. Gozzo, N.M. Crespo, M.d.S. Custodio, V. Lucyrio, E.M. de Jesus,  
985      and R.P. da Rocha. 2022. From a shapiro-keyser extratropical cyclone to the sub-  
986      tropical cyclone raoni: An unusual winter synoptic situation over the south atlantic  
987      ocean. *Quarterly Journal of the Royal Meteorological Society* 148(747): 2991–3009 .
- 988      Reboita, M.S., N.C.d.O. Nogueira, I.B.d.S. Gomes, L.L.d.C. Palma, and R.P.  
989      da Rocha. 2024. Assessment of a tropical transition over the southwestern  
990      south atlantic ocean: The case of cyclone akará. *Journal of Marine Science and  
991      Engineering* 12(11): 1934 .
- 992      Reed, R.J. and R.H. Johnson. 1974. The vorticity budget of synoptic-scale wave distur-  
993      bances in the tropical western pacific. *Journal of the Atmospheric Sciences* 31(7):  
994      1784–1790 .
- 995      Reed, R.J., D.C. Norquist, and E.E. Recker. 1977. The structure and properties of  
996      african wave disturbances as observed during phase iii of gate. *Monthly Weather  
997      Review* 105(3): 317–333 .
- 998      Rennick, M.A. 1976. The generation of african waves. *Journal of Atmospheric  
999      Sciences* 33(10): 1955–1969 .
- 1000      Rios-Berrios, R., P.M. Finocchio, J.J. Alland, X. Chen, M.S. Fischer, S.N. Stevenson,  
1001      and D. Tao. 2024. A review of the interactions between tropical cyclones and  
1002      environmental vertical wind shear. *Journal of the Atmospheric Sciences* 81(4):

- 1003        713–741 .
- 1004        Schmit, T.J., P. Griffith, M.M. Gunshor, J.M. Daniels, S.J. Goodman, and W.J.  
 1005        Lebair. 2017. A closer look at the abi on the goes-r series. *Bulletin of the American  
 1006        Meteorological Society* 98(4): 681–698 .
- 1007        Shimura, T., N. Mori, and T. Miyashita. 2024. Footprint of the air-sea momen-  
 1008        tum transfer saturation observed by ocean wave buoy network in extreme tropical  
 1009        cyclones. *Coastal Engineering* 191: 104537 .
- 1010        Silva, B.A., M.S. Reboita, L.M.M. Dutra, N.M. Crespo, and R.P. da Rocha. 2022.  
 1011        Ciclones subtropicais guará e lexi parte ii: processos físicos responsáveis pelas car-  
 1012        acterísticas subtropicais. *Revista Brasileira de Geografia Física* 15(01): 359–372  
 1013        .
- 1014        Sinclair, M.R. 1994. An objective cyclone climatology for the southern hemi-  
 1015        sphere. *Monthly Weather Review* 122(10): 2239–2256. [https://doi.org/10.1175/1520-0493\(1994\)122<2239:AOCCFT>2.0.CO;2](https://doi.org/10.1175/1520-0493(1994)122<2239:AOCCFT>2.0.CO;2) .
- 1016        Smith, P.J. 1980. The energetics of extratropical cyclones. *Reviews of Geo-  
 1017        physics* 18(2): 378–386 .
- 1018        Stoelinga, M.T. 1996, May. A potential vorticity-based study of the role of diabatic  
 1019        heating and friction in a numerically simulated baroclinic cyclone. *Monthly Weather  
 1020        Review* 124(5): 849–874 .
- 1021        Trenberth, K.E. 1978. On the interpretation of the diagnostic quasi-geostrophic omega  
 1022        equation. *Mon. Wea. Rev* 106(1): 131–137 .
- 1023        Vannière, B., M. Roberts, P.L. Vidale, K. Hodges, M.E. Demory, L.P. Caron, E. Scoc-  
 1024        cimarro, L. Terray, and R. Senan. 2020. The moisture budget of tropical cyclones in  
 1025        highresmip models: large-scale environmental balance and sensitivity to horizontal  
 1026        resolution. *Journal of Climate* 33(19): 8457–8474 .
- 1027        Veiga, J.A.P., A.B. Pezza, I. Simmonds, and P.L. Silva Dias. 2008. An analysis of the  
 1028        environmental energetics associated with the transition of the first south atlantic  
 1029        hurricane. *Geophysical Research Letters* 35(15) .
- 1030        Vianna, M., V. Menezes, A. Pezza, and I. Simmonds. 2010. Interactions between  
 1031        hurricane catarina (2004) and warm core rings in the south atlantic ocean. *Journal  
 1032        of Geophysical Research: Oceans* 115(C7) .
- 1033        Wood, K., W. Yanase, J. Beven, S.J. Camargo, J.B. Courtney, C. Fogarty, J. Fukuda,  
 1034        N. Kitabatake, M. Kucas, R. McTaggart-Cowan, et al. 2023. Phase transitions  
 1035        between tropical, subtropical, and extratropical cyclones: A review from iwtc-10.  
 1036        *Tropical Cyclone Research and Review* .
- 1037

- 1038 Wu, M.L.C., O. Reale, S.D. Schubert, M.J. Suarez, and C.D. Thorncroft. 2012.  
1039 African easterly jet: Barotropic instability, waves, and cyclogenesis. *Journal of*  
1040 *Climate* 25(5): 1489–1510 .
- 1041 Wu, Y.C., M.J. Yang, and R.F. Rogers. 2022. Examining terrain effects on the evo-  
1042 lution of precipitation and vorticity of typhoon fanapi (2010) after departing the  
1043 central mountain range of taiwan. *Monthly Weather Review* 150(6): 1517–1540 .
- 1044 Yokota, S., H. Niino, and W. Yanase. 2012. Tropical cyclogenesis due to breakdown of  
1045 intertropical convergence zone: An idealized numerical experiment. *Sola* 8: 103–106  
1046 .
- 1047 Yokota, S., H. Niino, and W. Yanase. 2015. Tropical cyclogenesis due to itcz break-  
1048 down: Idealized numerical experiments and a case study of the event in july 1988.  
1049 *Journal of the Atmospheric Sciences* 72(9): 3663–3684 .
- 1050 Zhan, R. and Y. Wang. 2012. Contribution of tropical cyclones to stratosphere-  
1051 troposphere exchange over the northwest pacific: Estimation based on airs  
1052 satellite retrievals and era-interim data. *Journal of Geophysical Research: Atmo-*  
1053 *spheres* 117(D12) .
- 1054 Zhao, B., G. Wang, J.A. Zhang, L. Liu, J. Liu, J. Xu, H. Yu, C. Zhao, X. Yu, C. Sun,  
1055 et al. 2022. The effects of ocean surface waves on tropical cyclone intensity: Numer-  
1056 ical simulations using a regional atmosphere-ocean-wave coupled model. *Journal of*  
1057 *Geophysical Research: Oceans* 127(11): e2022JC019015 .